A Curvature-Based Framework for Automated Classification of Meander Bends

Sergio Antonio Lopez Dubon[1], Alessandro Sgarabotto[2], and Lanzoni Stefano[3]

[1]University of Edinburgh
[2]University of Plymouth
[3]Dipartimento di Ingegneria, Idraulica, Marittima e Geotecnica, Universita´ di Padova, Padua, Italy

March 29, 2024

Abstract

River meanders are one of the most recurrent and varied patterns in fluvial systems. Multiple attempts have been made to detect and categorise patterns in meandering rivers to understand their shape and evolution. A novel data-driven approach was used to classify single-bend meanders. A dataset containing approximately 10 million single-lobe meander bends was generated using the Kinoshita curve. A neural network autoencoder was trained over the curvature energy spectra of Kinoshita-generated meanders. Then, the trained network was then tested on real meander bends extracted from satellite images, and the energy spectrum in the meander curvature was reconstructed accurately thanks to the autoencoder architecture. The meander spectrum reconstruction was clustered, and three main bend shapes were found associated with the meander datasets, namely symmetric, upstream-skewed, and downstream-skewed. The autoencoder-based classification framework allowed bend shape detection along rivers, finding the dominant pattern with implications on migration trends. By studying the shift in the prevailing bend shape over time, cutoff events were approximately forecast along the Ucayali River, whose migration was remotely sensed for 32 years. Overall, the method proposed opens the venue to data-driven classifications to understand and manage meandering rivers. Bend shape classification can thus inform restoration and flood control practices and contribute to predicting meander evolution from satellite images or sedimentary records.

A Curvature-Based Framework for Automated Classification of Meander Bends

Sergio Lopez Dubon[1], Alessandro Sgarabotto[2,3], and Stefano Lanzoni[4]

[1]School of Engineering, University of Edinburgh, Edinburgh, United Kingdom
[2]School of Geography, Earth and Environmental Sciences, University of Plymouth, Plymouth, United Kingdom
[3]School of Engineering, University of Birmingham, Birmingham, United Kingdom
[4]Department of Civil, Environmental and Architectural Engineering, University of Padova, Padova, Italy

Key Points:

- A curvature-based classification framework of meander bends was successfully trained over Kinoshita-generated meanders.
- By testing the trained framework over real meander bends, 3 classes were found, namely symmetrical, downstream-skewed, and upstream-skewed.
- The proposed framework detects the dominant shape class in river reaches and how this changes over time when cutoff events occur.

Corresponding author: Sergio Lopez Dubon, `Sergio.LDubon@ed.ac.uk`

Abstract

River meanders are one of the most recurrent and varied patterns in fluvial systems. Multiple attempts have been made to detect and categorise patterns in meandering rivers to understand their shape and evolution. A novel data-driven approach was used to classify single-bend meanders. A dataset containing approximately 10 million single-lobe meander bends was generated using the Kinoshita curve. A neural network autoencoder was trained over the curvature energy spectra of Kinoshita-generated meanders. Then, the trained network was then tested on real meander bends extracted from satellite images, and the energy spectrum in the meander curvature was reconstructed accurately thanks to the autoencoder architecture. The meander spectrum reconstruction was clustered, and three main bend shapes were found associated with the meander datasets, namely symmetric, upstream-skewed, and downstream-skewed. The autoencoder-based classification framework allowed bend shape detection along rivers, finding the dominant pattern with implications on migration trends. By studying the shift in the prevailing bend shape over time, cutoff events were approximately forecast along the Ucayali River, whose migration was remotely sensed for 32 years. Overall, the method proposed opens the venue to data-driven classifications to understand and manage meandering rivers. Bend shape classification can thus inform restoration and flood control practices and contribute to predicting meander evolution from satellite images or sedimentary records. **Keywords**: Meandering rivers; Automatic Classification; Wavelets; Model Transferability; Autoencoder; Pattern recognition

Plain Language Summary

Single-thread rivers commonly cut through alluvial floodplains with continuous sinuous curves. Classifying meanders provides a key to understanding their shape and, thus, learning how they have changed over time. A novel classification framework was proposed using a machine-learning model for pattern recognition in images. This model was trained over the curvature energy distribution within the meander bends generated from analytical relations. The classification framework was then tested over a set of real meander bends extracted from satellite images. The trained model grasped the most important features contained in curvature energy distribution, grouping the meander data set into three bend-shaped clusters, namely symmetric, upstream-skewed, and downstream-skewed. The proposed framework was then used to find the predominant bend class and its shifts during river migration, offering a different perspective on meander evolution. Bend shape classification can be used to guide restoration and flood control plans and predict meandering trends from satellite images or sedimentary records.

1 Introduction

Meander bends are patterns widespread in both fluvial and tidal systems (e.g., Leopold et al., 1964; Leuven et al., 2018; Finotello et al., 2020). While migrating on the alluvial plain, meander bends evolve by growing in amplitude, fattening, and skewing. Eventually, the sinuous loops, if too narrow, cut off starting a new course (e.g., Kleinhans et al., 2023).

Restoration practices often include re-introducing meanders to enhance biodiversity and mitigate flood peaks by promoting floodplain inundation and slowing down the flow (e.g., Wohl et al., 2015). River sinuosity associated with the presence of meanders favours the accommodation of organic matter, improving the stability of the riparian soil and reducing the impact of dam constructions (Ran et al., 2022). Moreover, meandering rivers, especially those migrating actively on floodplains, are more efficient in carbon sequestration than straight rivers, thus contributing to climate change mitigation (Repasch et al., 2021). Studies on static planform shapes and their classification can also improve our understanding of meander dynamics and give insights on paleochannels (e.g., Yan et al., 2021; Bellizia et al., 2022; Sgarabotto et al., 2024). Overall, the study of meander morphology can help to understand how meandering rivers evolve and provide insights for effective river management.

Bend geometries can be very complex. They include single-lobe bends and multi-lobe bends when adjacent bends merge, making it hard to detect the single-bends inflexion points and apexes unambiguously. Different classification frameworks have been proposed to address the complexity and variety of meandering patterns and help the understanding of their morphodynamics (Leopold et al., 1964; Howard & Hemberger, 1991; Lagasse et al., 2004; Güneralp et al., 2012; Lanzoni, 2022). Classifications serve various purposes, and their relevance depends on the ease of use, the possibility to analyse many different patterns, the ability to grasp the physical processes, and, more recently, the potential for automation (Buffington & Montgomery, 2013). In general, meander classifications can be grouped into qualitative approaches, based on shape matching, and quantitative approaches, which rely on bend parametrisation, bend evolution frameworks, spectral methods, or data-driven methods (Hooke, 2013).

The visual similarity between bends led to a classification in which the observed meanders are subjectively matched to shape prototypes (Brice, 1974; Ielpi & Ghinassi, 2014). To encompass even complex morphologies, the number of classes is progressively increased. For example, the four classes initially proposed by Brice (1973), were extended to 16 by Brice (1974) and further expanded to 70 by Hooke (1977). A simplification of this approach was put forward by Hooke and Harvey (1983), who, in addition to the shape matching, considered various simple mechanisms to account for evolution processes, such as free and confined mender migration, bend growth, lobbying, double heading, formation of new bends, cutoff, and retraction. The subjective nature of visual classification was later supported by objective shape assessments based on ensemble statistics of the planforms included between successive inflexion points of the channel axis. The bend shape was investigated by analysing geometrical features such as the radius of curvature, the cartesian and intrinsic lengths, the sinuosity, and the asymmetry index. Bend shapes were initially classified using single metrics, such as the sinuosity (Schumm, 1985) and the radius of curvature (Nanson & Hickin, 1983; Hickin & Nanson, 1984). Subsequently, shape characterisation was improved by considering multiple metrics. Slope, sinuosity, and width-to-depth ratio were used by Rosgen (1994) to characterise river systems. More recently, Russell et al. (2018) proposed to use a polygon built around a meander bend such that its sides were tangent to the meander centreline. The length of the meander centreline was normalised with the bend width, and the ratio between the area and perimeter of the polygon concurred to define the various meander classes. Nevertheless, all the aforementioned methodologies present two main problems. First, they are too complicated to encompass as many shapes as possible. Indeed, the geometrical metrics considered insufficient to characterise unambiguous single meander bends. In contrast, a suite of them can be used for the statistical characterisation of an entire river reach (Camporeale et al., 2005; Frascati & Lanzoni, 2009). Secondly, the great variety of meander shapes (e.g., Figure 1a-d) makes the above classification frameworks cumbersome to automate and test on a large meander dataset.

To overcome the issues of shape matching and bend parametrisation approaches, the bend evolution was described through simplified mechanistic models aimed to reproduce the variety of meander bends (Hooke & Harvey, 1983; Lagasse et al., 2004). In particular, the explanation of meander initiation through the bend instability mechanism (Ikeda et al., 1981; Blondeaux & Seminara, 1985) led to the formulation of numerous deterministic models of meander morphodynamics. Early models described the evolution of meander bends considering a linearised treatment of the morphodynamic problem, and using a simplified bank erosion law based on the difference in flow speed experienced at the outer and inner banks (Crosato, 1990; Seminara & Tubino, 1992; Seminara et al., 2001). Further mechanisms were subsequently added in this type of models, such as the occurrence of cutoffs (Howard & Knutson, 1984; Camporeale et al., 2008; Schwenk & Foufoula-Georgiou, 2016; Weisscher et al., 2019), the effects of height and sediment composition of the banks and

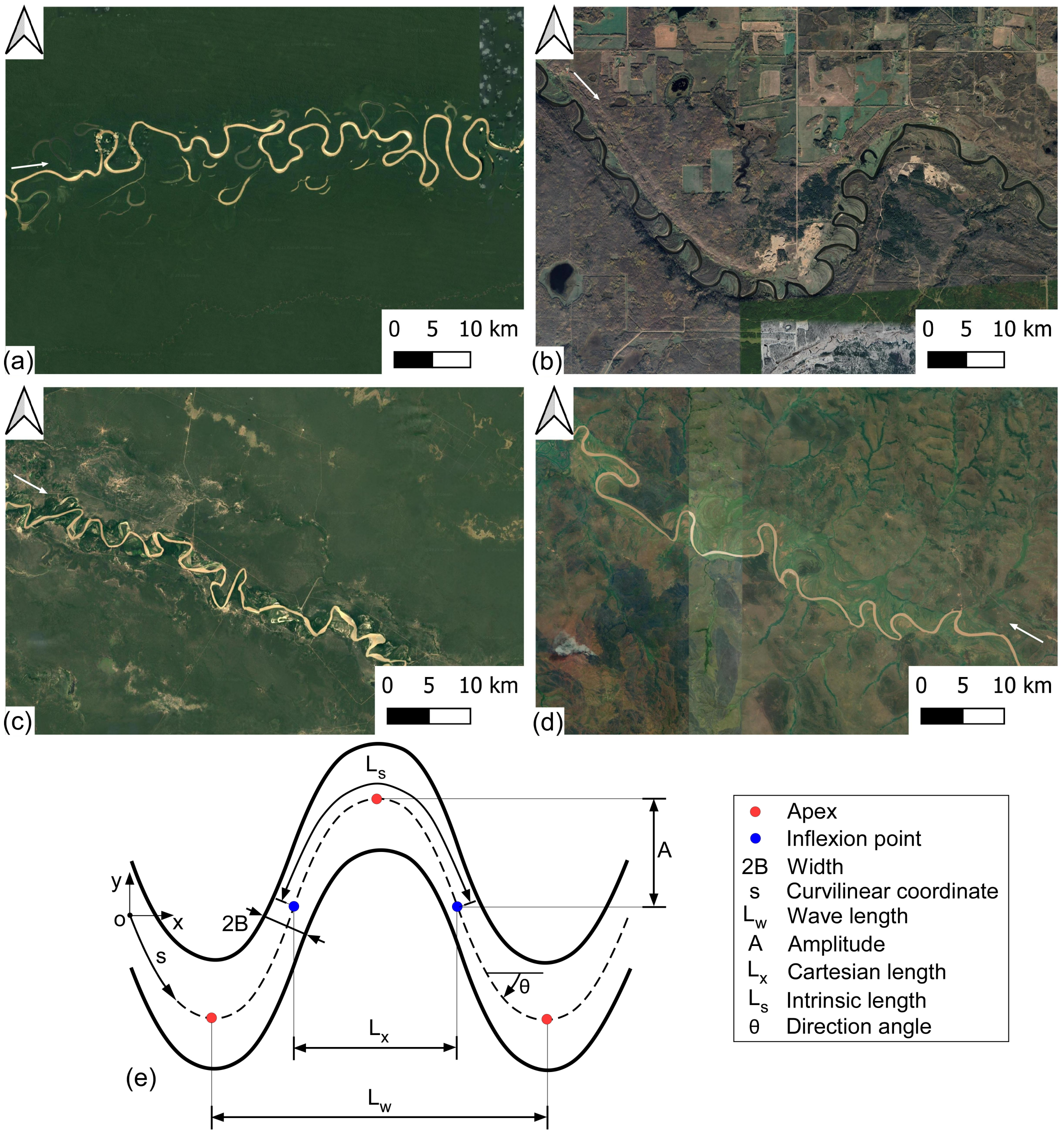

Figure 1. Satellite images of meandering patterns along the (a) Juruá (Brazil), (b) Beaver (Canada), (c) Bermejo (Argentina), and (d) Kwango (Angola/Congo) rivers. All the images were taken in May 2023: (a) and (c) were extracted from Bing Areal Maps; (b) and (d) were extracted from Google Satellite. (e) A schematic illustrating the main geometrical features of a meander bend.

the formation of slump blocks (Mosselman, 1998; Parker et al., 2011; Langendoen et al., 2016), the presence of channel width variations (Wu et al., 2011; Zolezzi et al., 2012; Frascati & Lanzoni, 2013; Lopez Dubon & Lanzoni, 2019), and the consequences of floodplain heterogeneity due to former river wanderings or geological constraints (Motta et al., 2012; Bogoni et al., 2017). If included in the modelling framework, riparian vegetation was found to reduce the shear stress distribution and affect bank erodibility, narrowing the stream and slowing down the migration process in the long-term (Sun et al., 2010; Camporeale et al., 2013; Weisscher et al., 2019; Ielpi et al., 2022). Linearised morphodynamic models were also used to characterise meander morphology in terms of the potential extension of the meander belt (Camporeale et al., 2005). Specifically, the ratio between the meander belt width and the channel width was used to define an entrenchment ratio that quantifies the overall propensity of a meandering river to migrate laterally. This metric was also used in Rosgen classification (Rosgen, 1994).

An attempt was put forward to integrate the shape characterisation with hydro-morphodynamic information by Bolla Pittaluga and Seminara (2011) and Schwenk et al. (2015). In particular, Bolla Pittaluga and Seminara (2011) proposed a mechanistic classification of meander bends relying on four dimensionless groups quantifying the relative importance of friction as compared to local inertia (Σ), longitudinal convection ($\mathfrak{L}$), centrifugal inertia (δ), and lateral convection $\mathfrak{b}$. These four parameters are defined as:

$$\Sigma = \frac{D_u}{L_{T0}\sqrt{C_{fu}}}, \quad \mathfrak{L} = \frac{D_u}{L\sqrt{C_f u}}, \quad \delta = \frac{D_u}{R_0\sqrt{C_{fu}}}; \quad \mathfrak{b} = \frac{D_u}{B\sqrt{C_{fu}}} \tag{1}$$

where D_u is the uniform flow depth, C_{fu} is the corresponding friction coefficient, B is the half-width of the channel, L_{T0} is a characteristic convective scale defined as the distance covered by a fluid particle moving with a velocity U_u in the time scale T_0, L is a characteristic spatial scale (e.g. the meander wavelength), and R_0 is an appropriate radius of curvature. The typical values of these groups were extracted from a real meanders database (Lagasse et al., 2004). Based on the values attained by the above parameters, mildly curved bends were found to be quite common. Specifically, half of the meanders analysed by Bolla Pittaluga and Seminara (2011) exhibited a relatively small value (below 0.18) of the parameter δ. Even though classifications of meander shapes relying on hydraulic parameters are not widely adopted, various studies have highlighted the strong link between meander shape morphology and its formative dynamics (e.g., Schwenk et al., 2015; Guo et al., 2019).

Meandering morphology has also been characterised through spectral analysis, considering flow direction or channel axis curvature (Howard & Hemberger, 1991). Indeed, bend curvature provides valuable insight into meander shape, given its strong influence on the flow field, sediment dynamics, and ultimately, on the rate of bend migration (Güneralp & Rhoads, 2008; Finotello et al., 2018; Donovan et al., 2021). Meandering patterns were also mimicked through a random walk process, where changes in direction were assumed as independent random variables, representing the effects of disturbances to the system (Langbein & Leopold, 1966). In addition, Langbein and Leopold (1966) argued that changes in meandering direction can be well approximated by a sine-generated curve that minimises the variance from the stable state defined by the mean downstream direction. By describing the meandering process as completely random, the meandering path degenerates into a straight line when disturbances to the system are removed. To overcome this issue, river meanders were treated as deterministic oscillations with a random component attributed to a variable floodplain composition, affecting the planform angle (Langbein & Leopold, 1966; Howard & Hemberger, 1991) or vertical bank elevation (Lazarus & Constantine, 2013). More recently, meander morphology was investigated by analysing the energy spectrum of curvature distribution in a bend by wavelets (Gutierrez & Abad, 2014; Zolezzi & Güneralp, 2015).

Despite the numerous attempts outlined above, an automatic, objective classification of meander bends has yet to be developed. Machine learning offers techniques to find patterns in large datasets, proving its versatility in many geomorphology applications, such as the detection of fluvial geomorphic features from satellite images (Bozzolan et al., 2023).

The present study proposes a physics-based, data-driven method to automatically classify meander bends, based on the energy spectrum of the curvature distribution. This approach is deemed to overcome the shortcomings of existing classification methods.

The rest of the paper is structured as follows. Section 2 presents the methodologies used to generate synthetic meander planforms and extract real meander shapes from satellite images. This section also outlines the development of the data-driven unsupervised classification framework, relying on the energy spectrum of the bend curvature distribution. Section 3 presents the classification results obtained for real meander bends. In section 4, the classification results are discussed in terms of meander morphodynamics, also considering the specific case of a reach of the Ucayali River. Finally, section 5 reports the conclusions.

2 Methods

The automated classification framework developed in this study exploits the information contained in the spatial distribution of channel axis curvature. We propose to summarise this information through its wavelet spectrum, which is then used to automatically identify the typology of a given meander bend. A neural network autoencoder was trained on the wavelet energy spectra extracted from a large series of synthetic meanders. The classification procedure based on this autoencoder was subsequently tested on an independent set of synthetically generated bends and real meander shapes extracted from satellite images.

The development of the overall framework included six steps (Figure 2). First, single-bend meanders were generated from the Kinoshita curve for both training and testing purposes. Next, the continuous wavelet transform was applied to the spatial distribution of channel axis curvature for each bend, computing the corresponding total energy wavelet spectrum. Third, the images of the energy spectra were used to train an autoencoder which compresses the information contained in each image, locates it in a latent two-dimensional space and eventually reconstructs it. This autoencoder was then tested over an independent set of synthetically generated bends, as well as on real single-bend meanders. Fifth, the K-means algorithm was used to find out the optimal number of clusters through which the real meanders can be grouped in the latent space. Finally, the cluster centroid was used to represent the characteristic shape of the cluster, regardless of bend amplitude and wavenumber. Below, we summarise the key features of the various steps.

2.1 Synthetically-generated meanders

The synthetic sets of meander planforms used first to train and subsequently to test the automatic classification procedure were generated according to the so-called Kinoshita curve (Kinoshita, 1961). This curve represents a slightly modified version of the sine-generated curve of (Langbein & Leopold, 1966), and can describe a rich spectrum of meander shapes (Seminara et al., 2001; Vermeulen et al., 2016; Seminara et al., 2023), from single-lobe meanders, which have only two inflexion points of the curvature distribution, to compound meanders, with multiple inflexion points. Denoting by s the intrinsic coordinate of the channel axis and L_w the meander wavelength (Figures 1e and 2a), the Kinoshita curve expresses the angle that the tangent to the channel axis forms with that of the valley as

$$\theta = \theta_1 \sin(\lambda s) + \theta_{3r} \cos(3 \lambda s) + \theta_{3i} \sin(3 \lambda s), \tag{2}$$

where $\lambda = 2\pi/L_w$ is the meander wavenumber. The spatial distribution of the channel axis curvature $c(s)$ is readily computed as

$$c(s) = -\frac{d\theta}{ds} = c_0 \left[\cos(\lambda s) - c_F \sin(3 \lambda s) + c_S \cos(3 \lambda s)\right], \tag{3}$$

with $c_0 = \lambda\theta_1$, $c_F = 3\,\theta_{3r}/\theta_1$ and $c_S = 3\,\theta_{3i}/\theta_1$ dimensionless parameters controlling the bend shape. In particular, c_F is associated with the bend fattening, whereas c_S determines whether the bend is skewed upstream or downstream.

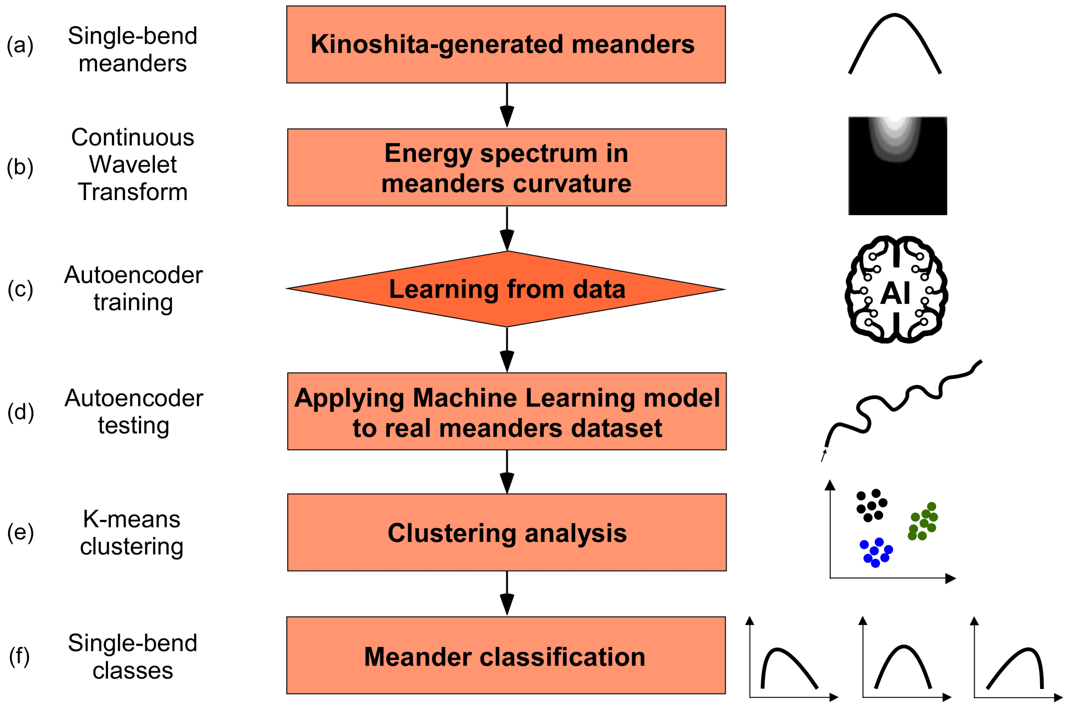

Figure 2. Flowchart illustrating the six steps involved in developing the automated classification procedure of meander bends based on the energy spectrum of the spatial distribution of channel axis curvature.

The intrinsic coordinate s and the cartesian coordinates (x, y) are related together by the transformations

$$\frac{dx}{ds} = \cos\theta(s), \qquad \frac{dy}{ds} = \sin\theta(s), \tag{4}$$

allowing to reconstruct the bend shape in the (x, y)-plane.

To produce a meaningful set of planform geometries, the values of the parameters θ_1, θ_{3r} and θ_{3i} were chosen taking advantage of the real meander dataset of Lagasse et al. (2004). A statistical analysis indicated that the wavenumber of meanders can be described by a Probability Distribution Function (PDF) based on the gamma function Γ, namely

$$f_\Gamma(\xi) = \frac{\xi^{(\gamma_a - 1)}}{\gamma_b^{\gamma_a}\,\Gamma(\gamma_a)} \exp\left[-\left(\frac{\xi}{\gamma_b}\right)\right], \tag{5}$$

where the best-fit values of the coefficients γ_a and γ_b, are equal to 12.728 and 0.0265, respectively. These values lead to a coefficient of determination R^2 equal to = 96.13%, and a Bayesian Information Criterion (BIC) of -2.551 $\cdot 10^2$.

The wavenumbers of the Kinoshita-generated meanders were selected by randomly sampling from the PDF (5). On the other hand, as no information was available about the statistical distribution of the parameters θ_1, θ_{3r} and θ_{3i}, their values were randomly sampled from a uniform PDF using a pseudo-random number generator function (Harris et al., 2020). Moreover, to avoid intertwined loops, the coefficients θ_{3r} and θ_{3i} were selected in the range $[-1, 1]$ assuming a zero mean value. Finally, the amplitude coefficient θ_1 was chosen in the range $[4/\pi - 1, 4/\pi + 1]$, with a mean value equal to $4/\pi$.

Each bend composing a single-lobe meander, or a compound bend meander, was identified by considering two consecutive inflexion points. Each bend was then resampled to contain the same number of points (i.e., 201), rotated to align its extremes with the x-axis, and saved on a specific dataset. This dataset, containing approximately 10 million of synthetically-generated bends, was subsequently divided into two independent sub-datasets, used afterwards for the training (8.5 million bends) and the testing (1.5 million bends) of the automatic classification procedure. The frequency distributions of the wavenumber λ and the parameters θ_1, θ_{3r} and θ_{3i} used in the Kinoshita curve are shown in Figure S1 of the Supporting Information.

2.2 Wavelet energy spectrum

The wavelet transform allows the analysis of temporal or spatial signals with a flexible time-frequency (or space-frequency) window (mother wavelet) that adjusts automatically, narrowing for high-frequency oscillations and widening for low-frequency oscillations (Antoine et al., 2004; Addison, 2018; Tary et al., 2018). In the present study, we have applied this analysis to the spatial distribution of the bend curvature $c(s)$.

The mother wavelet can, in general, be written as (Foufoula-Georgiou & Kumar, 1994):

$$\psi_{b,a}(s) = \frac{1}{\sqrt{a}}\,\psi\Big(\frac{s-b}{a}\Big), \tag{6}$$

where a is a positive scale parameter, and b is a real space parameter. The scale parameter controls the frequency by which the wavelet samples the curvature distribution, leading to either a dilatation ($a > 1$) or a contraction ($a < 1$) of the mother wavelet. The space parameter determines the sampling position along s of the mother wavelet.

The continuous wavelet transform of the curvature distribution is defined as

$$\Psi_c(b,a) = \frac{1}{\sqrt{a}}\int_{-\infty}^{\infty} c(s)\,\overline{\psi}_{b,a}(s)\,ds, \tag{7}$$

where an overbar denotes complex conjugate.

In general, a wavelet $\psi(s)$ and, in particular, the mother function must satisfy various conditions. It must have compact support or sufficiently fast decay to obtain localisation in space and have a zero mean,

$$\int_{-\infty}^{\infty}\psi(s)\,ds = 0. \tag{8}$$

Moreover, it must satisfy the admissibility condition.

$$C_\psi = 2\int_0^{\infty}\frac{\big|\widehat{\psi}(k)\big|^2}{k}\,dk < \infty, \tag{9}$$

where k is the wavenumber (i.e., the spatial frequency), and $\widehat{\psi}(k)$ is the Fourier transform of ψ, defined as

$$\widehat{\psi}(k) = \int_{-\infty}^{\infty}\psi\,(s)\,e^{-i\,k\,s}\,ds. \tag{10}$$

Mother wavelets can be defined in either the real or complex domain. In the case of complex wavelets, an additional requirement is that $\widehat{\psi}(k)$ must be real and vanish for negative wavenumbers ($k \leq 0$). This type of wavelet, referred to as progressive, enhances the ability to identify singularities in the signal.

The inverse wavelet transform, allowing the reconstruction of the original curvature distribution, is defined as

$$c(s) = \frac{2}{C_\psi}\int_0^{\infty}\Big[\int_{-\infty}^{\infty}\Psi_c(b,a)\,\psi_{b,a}(s)\,db\Big]\,\frac{da}{a^2}. \tag{11}$$

It is easily demonstrated that the continuous wavelet transform is an energy-preserving transformation ensuring that (Foufoula-Georgiou & Kumar, 1994)

$$E_c = \int_{-\infty}^{\infty} \left|c(s)\right|^2 = \frac{2}{C_\psi} \int_0^{\infty} \int_{-\infty}^{\infty} \left|\Psi_c(b,a)\right|^2 db \, \frac{da}{a^2}. \tag{12}$$

The quantity $\left|\Psi_c(b,a)\right|^2 / (C_\psi \, a^2)$ on the right-hand side of (12) can be interpreted as an energy density function on the (a,b)-plane, representing the energy on the scale interval Δa and spatial interval Δb, centred around the scale a and the position b. The quantity E_c thus quantifies the total energy in the wavelet spectrum of $c(s)$.

In this study, the PyWavelets Python package (Lee et al., 2019) was used to compute the continuous wavelet transform and the Mexican Hat.

$$\psi(s) = \frac{2}{\sqrt{3}\,\pi^{1/4}}(1-s)e^{-s^2/2} \tag{13}$$

was employed as mother wavelet.

2.3 Autoencoder

The total energy E_c of the wavelet spectrum for the channel axis curvature of each bed was represented through a greyscale image, with values ranging from 0 (black) to 256 (white) and a resolution of 64x64 pixels (Figure 2b). This simplified representation allowed the use of a smaller autoencoder with faster training.

In particular, we used a convolutional neural network autoencoder, consisting of a connected encoder and decoder. The encoder compresses each image into a low-dimensional latent representation while retaining as much essential information as possible from the high-dimensional initial space (Kingma & Welling, 2022). The decoder handles each latent space representation and reconstructs an output image that closely resembles the original input one (Goodfellow et al., 2016). The adopted autoencoder requires no supervision while training (Tschannen et al., 2018), and allows an efficient clustering in the latent space (Chadebec & Allassonniere, 2022).

The overall autoencoding process can be represented as

$$E_c = \mathcal{F}\big[\mathcal{G}(E_c)\big], \tag{14}$$

where $\mathcal{G}$ is the encoding function, and $\mathcal{F}$ is the decoding function. The neuronal networks associated with these two functions are trained such that

$$\underset{\mathcal{F},\mathcal{G}}{\operatorname{argmin}} \, \frac{1}{N} \sum_{i=0}^{N} \Delta\big\{E_{ci}, \mathcal{F}\big[\mathcal{G}(E_{ci})\big]\big\}, \tag{15}$$

where, N is the number of images used for the training, Δ is a loss function, defined as the binary cross-entropy measuring the binary logarithmic loss between predicted and true values (Creswell et al., 2017), and $\underset{\mathcal{F},\mathcal{G}}{\operatorname{argmin}}$ denotes the set of values of $\mathcal{F}$ and $\mathcal{G}$ for which the summation attains its minimum value.

The overall architecture of the autoencoder is summarised using the Visual Keras package (Gavrikov, 2020), as shown in Figure 3. The encoder consisted of a series of convolutional two-dimensional neural layers. Batch normalisation and flattening layers were used to encode the available information in a latent two-dimensional space. The decoder employed a series of transposed two-dimensional convolutional neural layers, followed by a batch normalisation layer. A convolutional two-dimensional neural layer was finally used to obtain the reconstructed image of the energy spectrum.

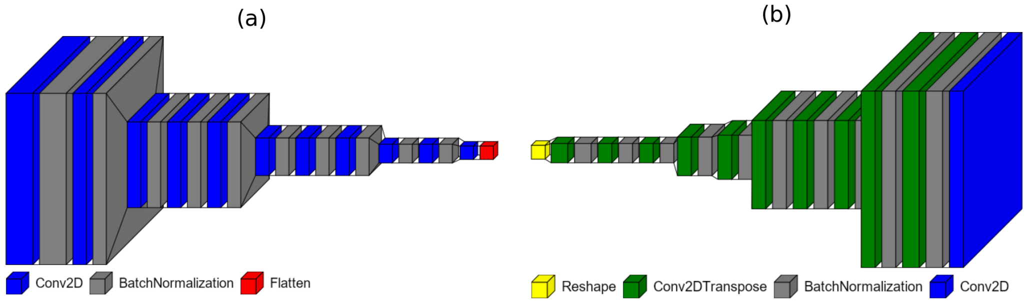

Figure 3. Autoencoder architecture. (a) Encoder and (b) Decoder.

The autoencoder was trained using the open-source TensorFlow software (Abadi et al., 2015). The bend curvature distributions computed from the Kinoshita-generated dataset were split into two independent subsets: 85% of bend curvature distributions were used for training, and the remaining 15% for validation. The error function selected for evaluating the correctness of the reconstructed images was a binary cross entropy function (Ruby et al., 2020), the binary loss being equal to 0 for a perfect model.

2.4 Clustering

The K-means algorithm (Brunton & Kutz, 2019) was used to find the optimal number of clusters characterising the image representation of E_c in the latent space. This optimal number was obtained by partitioning the data set into N_k groups S_i, such that the sum of squared deviations of the partitions is minimised. Denoting by $\mathcal{S}$ the generic partition, the function to be minimised is the within-cluster sum of squares $WCSS$, which can be formally expressed as (Kriegel et al., 2017)

$$WCSS = \sum_{S_i \in \mathcal{S}} \sum_{j=1}^{N_d} 2 \left|S_i\right| \sum_{\boldsymbol{x} \in S_j} (x_{ij} - \mu_{ij}). \tag{16}$$

Here, μ_{ij} is the mean coordinate of the cluster i in dimension j, $\left|S_i\right|$ is the cluster size, and the last summation defines the cluster variances. The minimisation of the function (16) was carried out through the Python package Scikit-Learn (Pedregosa et al., 2011).

2.5 Real meanders

The data-driven classification framework was first tested on an independent set of synthetically-generated bends, and then used to classify a set of 7521 real meander bends extracted from the datasets of Sylvester et al. (2019) and Lopez Dubon and Lanzoni (2019). The full list of the 32 meandering river reaches considered in the analysis is reported in Table S1 of the Supporting Information. Both datasets provide river planforms obtained by loading Google Earth maps in QGIS, zooming in on the river stretch of interest, drawing polylines along the river banks, and determining the centreline as the curve equidistant from each bank. This latter curve was smoothed out through a Savitzky-Golay filter (Savitzky & Golay, 1964) and a denoising wavelet filter (van der Walt et al., 2014) to reduce as much as possible spurious fluctuations when computing numerically the channel axis curvature.

The curvature was calculated by discretising the derivative $d\theta/ds$ in equation (3) through a second-order accurate central difference scheme for interior points, and either first or second-order accurate one-sided (forward or backward) differences at the boundaries, using the gradient function from the Python package numPy (Harris et al., 2020).

The along-river curvature distribution was then used to identify the inflexion points, where the curvature changed sign, and the bend apexes, where the curvature reached its maximum or minimum value. The position of inflexion points was finally used to recognise the sequence of single-lobe bends composing the river reach.

The noise in the numerically computed curvature can induce some small oscillations around zero and, consequently, the detection of spurious inflexion points. To avoid this problem only bends with a cartesian length L_x (Figure 1e) exceeding 5-8 the mean channel width, B_{mean}, were retained. Each single-lobe bend was eventually rotated to align the two inflexion points along the reference x-axis, and the platform was represented in the dimensionless cartesian plane $(x/B_{mean}, y/B_{mean})$.

Figure 4. (a) Localisation of the meandering rivers extracted from satellite images. The data refer to Lopez Dubon and Lanzoni (2019) except those with the superscript $*$ which refer to Sylvester et al. (2019). (b)-(j) Examples of parts of the meandering rivers extracted.

3 Results

Figure 5 shows an example of the automated classification procedure applied to a real river bend. In particular, Figure 5 (a) reports the planform of the bend plotted in the dimensionless cartesian plane, while the corresponding dimensionless curvature is plotted in Figure 5 (b) as a function of the curvilinear coordinate of the bend axis, scaled by its maximum length, s/s_{max}. The greyscale image of the total energy wavelet spectrum of the curvature distribution is reported in Figure 5 (c). Finally, Figure 5 (d) shows the correspondent image reconstructed through the trained autoencoder. The reconstructed image appears to capture the striking features of the original image. Overall the autoencoder performance in reconstructing the real meander data set resulted in a binary cross-entropy loss of just 0.1578. This close-matching reconstruction ensures a meaningful representation of the spectrum in the latent space, where compression of the information embedded in the spectrum facilitates cluster analysis.

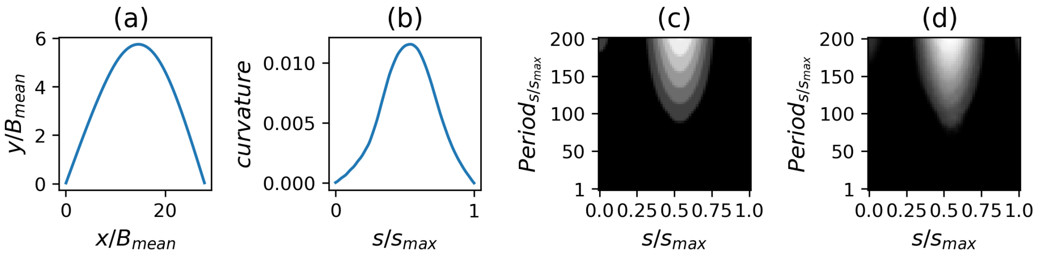

Figure 5. Example of application of the autoencoder to a real meander bend. (a) Bend shape plotted in the dimensionless plane (x/B_{mean},y/B_{mean}); (b) along-bend distribution of the channel axis curvature; (c) greyscale image of the total energy of the correspondent wavelet spectrum, with resolution 64×64 pixels and values ranging from 0 (black) to 256 (white); and (d) autoencoder reconstruction of the image.

As a preliminary step to the cluster analysis in the latent space, an additional criterion was applied to eliminate almost flat bends, typically associated with the very early evolution of a meander or multiple-lobe bends, which are not considered in the present analysis. Indeed, the energy spectrum of a nearly flat bend can be quite complicated, adding noise to the clustering procedure and making it less effective. Following Leopold and Wolman (1957), we assumed that bends belonging to a meandering reach have a sinuosity σ, defined as the ratio of intrinsic to cartesian length, larger than 1.5. The total number of meandering bends to be classified thus reduced from 7521 to 1911. The application of the K-means algorithm to this set of bends in the latent space yielded a number of clusters equal to 3. Increasing this number did not produce any significant improvement in minimising the within-cluster sum of squares defined by (16), as shown by Figure S2 in the Supporting Information.

Figure 6 summarises the results of the cluster analysis in the two-dimensional latent space, where three distinct clusters are discernible (Figure 6a). The bend shapes in the dimensionless plane $x/B_{mean}, y/B_{mean}$ corresponding to the three centroids are plotted in Figure 6b,c,d. They represent the characteristic bend shape typical of each cluster. Cluster C1 is characterised by symmetrical bends (Figure 6b), whereas clusters C2 and C3 are composed of downstream-skewed (Figure 6c) and upstream-skewed (Figure 6d) bends, respectively. The majority of data falls into cluster C1 (44% bends), followed by cluster C2 (36% bends) and cluster C3 (20% bends). On the other hand, the data dispersion within each cluster, defined as the ratio of standard deviation of the distance from the cluster centroid to the mean, is greater for cluster C3 (3.271), followed by cluster C2 (2.356), and cluster C1 (2.292).

The percentages of each bend type contained in the 32 river reaches considered in the present study are shown in Figure 7. Symmetrical bends (C1) prevail in 22 of the 32 river

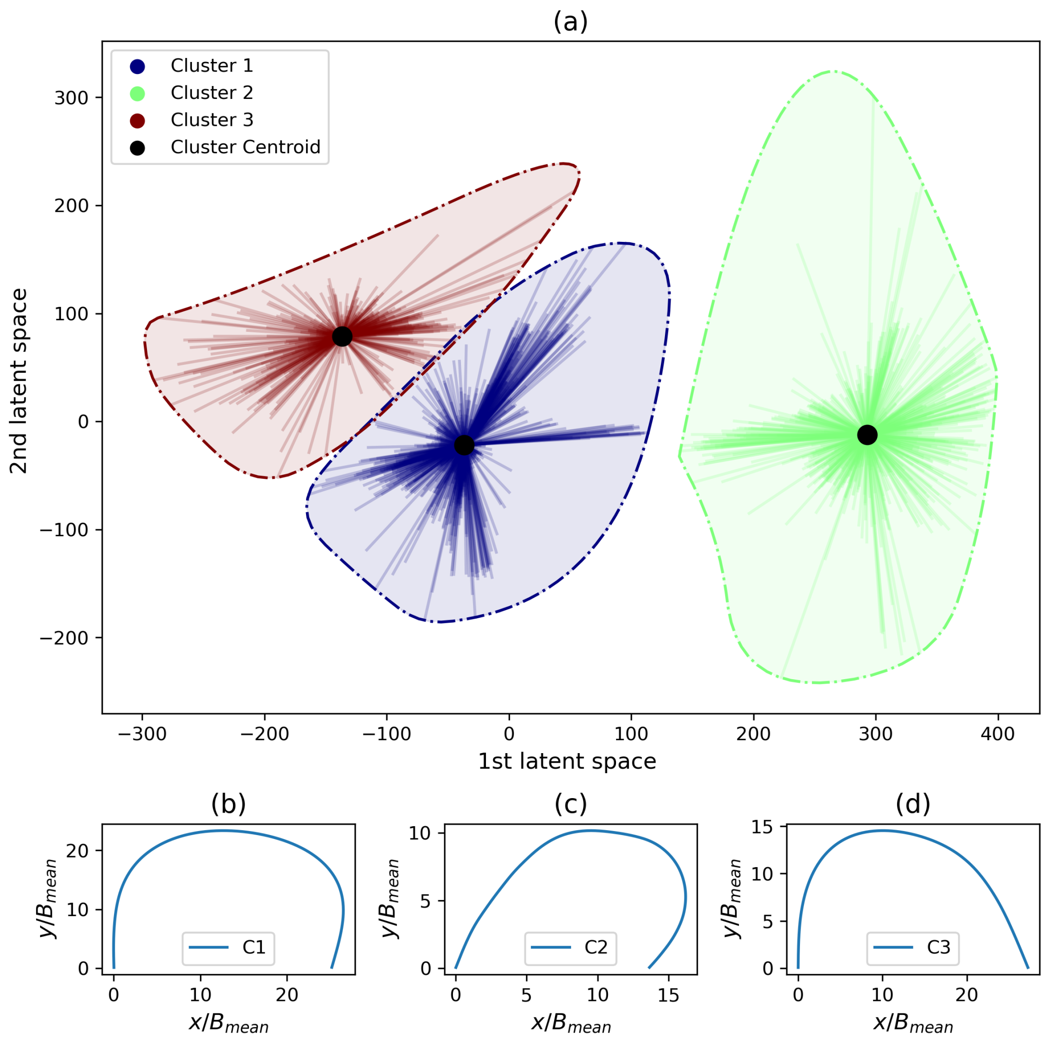

Figure 6. (a) Results of the cluster analysis in the two-dimensional latent space. Bend shapes corresponding to the centroid of (b) cluster C1, (c) cluster C2, and (d) cluster C3. The solid lines within each cluster connects each point to its centroid giving a visual representation of the cluster dispersion. The dashed-line connects the points located farther away from the centroid showing the cluster boundary.

reaches, whereas 10 out of 32 rivers exhibit a predominance of downstream-skewed bends. None of the investigated rivers had a predominance of upstream-skewed bends.

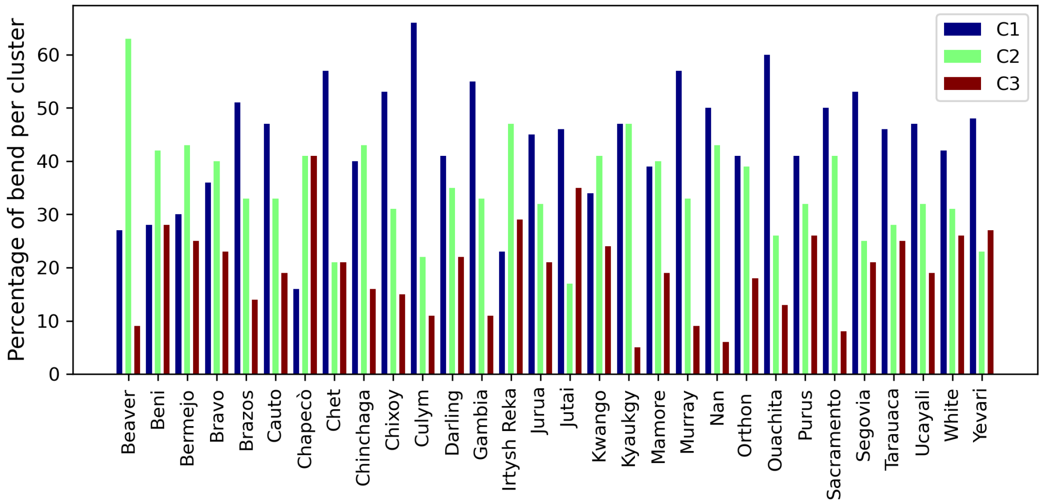

Figure 7. Percentages of the three bend types (C1, symmetrical; C2, downstream skewed; and C3, upstream skewed) emerging from the clustering analysis are reported for each of the meandering rivers reaches, as localised in Figure 4.

4 Discussion

The use of the Kinoshita curve (equation 2) was fundamental to produce a sufficient amount of data for training the autoencoder. This is particularly relevant, considering the vast effort required to extract river planforms from satellite images, as well as the river width needed for normalisation and comparison (Finotello et al., 2018). Moreover, the values of the loss function used to evaluate the autoencoder (0.1313 and 0.1312 for the training and evaluation set, respectively) indicate that, when applied to real rivers, the information lost in the latent space is reasonably small. This result confirms the reliable reconstruction of most of the energy spectrum images and, hence, a successful transfer of knowledge from the synthetic data used for training to real data.

Even though real bends with a sinuosity smaller than 1.5 were excluded from the classification analysis, some peculiar bend shapes remained included in the dataset. A few examples are shown in Figure 8a. Essentially, they are bends with small amplitude A as compared to their cartesian wavelength L_x, and relatively high sinuosity. To identify these particular bends, we introduces an Index of Maturity (I_M) defined as

$$I_M = \frac{A}{L_x}. \tag{17}$$

The values of the sinuosity and the Maturity Index for each meander bend are shown in Figure 8 (b), including all the bends extracted from the various river reaches, independently of the sinuosity. The point cloud seemingly has a lower-limit boundary that depends on the Maturity Index. This boundary has a shape that can be reasonably approximated though the parabola

$$\sigma = 2\, I_M \sqrt{1 + \frac{1}{4 I_M^2}}. \tag{18}$$

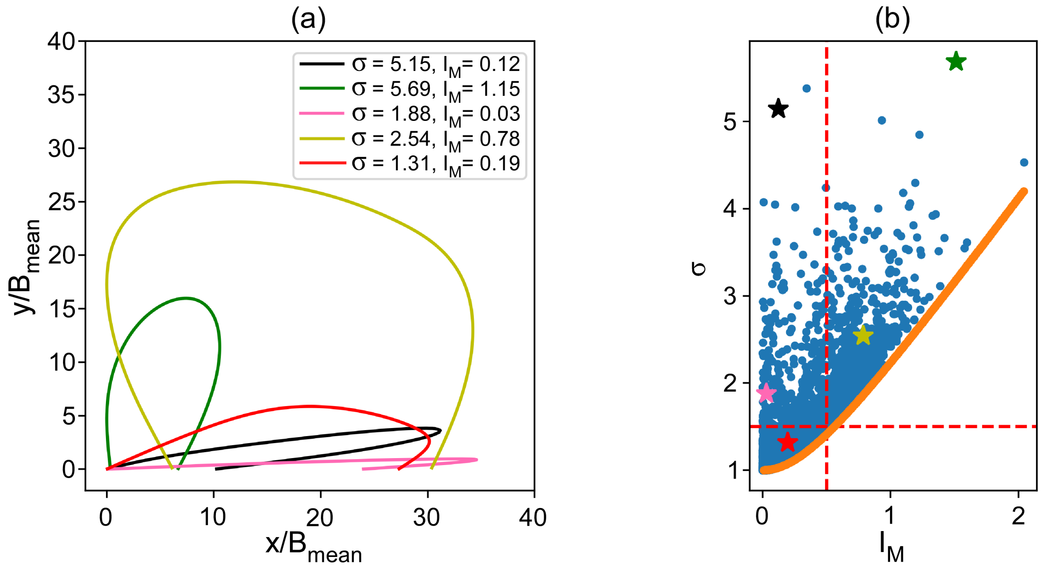

Figure 8. (a) Examples of the dependence of bend shapes from the values of σ and I_M. (b) The bend sinuosity σ is plotted as a function of the maturity index I_M for all the bends extracted from the investigated river reaches.

Figure 8 suggests that both the sinuosity and the Maturity Index can be used to identify bends with relatively uncommon shapes. Bends with $\sigma < 1.5$ are assumed to belong to nearly straight reaches, according to the classification proposed by Leopold and Wolman (1957). The line $\sigma = 1.5$ intercepts the lower-limit boundary for $I_M \simeq 0.56$. This latter value can be used to discriminate bends with small amplitude as compared to the wavelength ($I_M \lesssim 0.5$), leading to the peculiar shapes shown in Figure 8(a). This type of bends represents 25.4% of the total bends analysed. Excluding these bends from the cluster analysis does not change significantly the classification outputs. The number of clusters remains still equal to 3, with shapes representative of the corresponding centroids remarkably similar to those shown in Figure 6(b)-(d) (see Figure S3 in the Supporting Information). The criterion based on a lower threshold for I_M essentially identifies uncommon, nearly flat shapes, which have a limited overall impact on the automated classification procedure.

The sinuosity has a major role in identifying the degree of evolution of a given bend. Low-sinuosity bends usually represent the early stages of evolution, whereas high values of sinuosity are likely associated with bends in a more advanced stage of evolution. The statistical analysis carried out by Bolla Pittaluga and Seminara (2011) revealed that the meander bends in the database of Lagasse et al. (2004) have a median sinuosity of 1.7 and a standard deviation of 0.4. Bends with high sinuosity ($\sigma \gtrsim 3 - 3.5$) are likely to be relatively infrequent. This fact is confirmed by Figure 9, showing the box plot characterisation of the sinuosity distribution within each of the three clusters identified by the automated classification procedure. The values of the median sinuosity σ_m agree with those estimated for the database of Lagasse et al. (2004), with some slight variations from one cluster to another. In particular, the higher median value is observed for downstream-skewed bends (cluster C2, $\sigma_m = 2.014$), the smallest median value characterises upstream-skewed bends (cluster C3, $\sigma_m = 1.720$), while symmetrical bends (cluster C1) have $\sigma_m = 1.906$. The data dispersion, measured through the distance between the upper and lower quartiles (Interquartile Range, IQR), is highest for the downstream-skewed bends ($IQR = 0.758$), whereas upstream-skewed bends have the lowest degree of variation ($IQR = 0.305$). The trend of the sinuosity distribution for symmetrical bends is intermediate between the other two classes. Each cluster shows several upper outliers, i.e, larger than 1.5 times the interquartile range. In contrast, lower outliers are invariably absent. This absence is due to the choice of excluding bends with sinuosity lower than 1.5. The smallest number of outliers (6/435, $\sim$ 1.5%) is observed for upstream-skewed bends (C2, whereas the largest number (41/858, $\sim$ 5%) characterises the symmetrical bends (C1), which can be considered as a transition pattern between upstream-skewed (C3) and downstream-skewed (C2) bends (or vice versa).

The above results may be partly explained in light of existing theoretical studies of river meandering. According to the nonlinear bend instability analysis performed by Seminara et al. (2001), and confirmed by the results of numerical simulations up to incipient cutoff conditions (Lanzoni & Seminara, 2006), symmetrical bends mainly form during the initial evolution stages of a train of meanders developing along an initially straight, slightly-perturbed channel. In this phase, it is the first harmonic of the curvature, i.e. associated with the term $\cos(\lambda\, s)$ of equation (3), which grows almost linearly in time. The occurrence of skewed bends arises at a later stage of evolution due to slower nonlinear growth of the third harmonic $\cos(3\,\lambda\, s)$. During the first linear phase, the meander length increases slowly, while meander elongation is faster during the second phase, leading to the formation of fattened and skewed meander shapes. Bend amplification is initially quite slow, increases reaching a maximum, and then decreases slowly up to incipient cutoff conditions, as also observed in the field by Nanson and Hickin (1983). Conversely, the rate of lateral bend migration, which is quite fast at the beginning of the evolution, tends to progressively slow down up to almost vanishing before a neck cutoff. The direction of bend skewing is dictated by the morphodynamic regime characterising the river reach. This regime depends on the value of the width-to-depth ratio β with respect to its resonant value β_R. This latter value, in turn, is controlled by the Shields stress, τ_*, and the sediment grain size scaled with the uniform flow depth, d_s (Seminara & Tubino, 1992). For values of $\beta < \beta_R$ (sub-resonant regime), bends are upstream skewed and migrate downstream. Conversely, in the super-resonant regime ($\beta > \beta_R$), bends are downstream skewed and migrate upstream. As a meandering reach evolves, changes in the average reach slope, either due to the elongation of meander bends as they progressively grow or the shortening of the river path resulting from cutoffs, lead to variations of the reach-averaged values of β, and well as τ_* and d_s and, consequently, β_R. This can induce a change of the morphodynamic regime for values of β close to β_R, promoting the development of symmetrical bends (Zolezzi et al., 2009).

Within this general theoretical framework, higher variations in the sinuosity likely indicate the presence of a larger number of bends at different stages of evolution and, consequently, a potentially more dynamic river reach. Symmetrical bends can be associated to either relatively young evolution stages (e.g., those characterising a recently straighten, weakly sinuous reach) or to more advanced, higher sinuosity stages, as those linked to the change in morphodynamic regime when the evolving river reach approaches resonant conditions. Symmetrical bends may also be part of meanders with multiple loops (i.e., including multiple inflexion points), not accounted for in the present automated classification framework, which assumes a meander always delimited by two consecutive inflexion points of the channel axis curvature. The various origins of symmetrical bends may explain the greater number of outliers exhibited by the C1 cluster. Skewed bends, on the other hand, should, in general, represent more advanced stages of meander evolution, associated with higher values of sinuosity. This is indeed verified in Figure 9 for downstream-skewed bends but not for upstream-skewed bends, which have a median sinuosity also smaller than that of symmetrical bends. On the other hand, the number of upstream-skewed bends (distinctive of sub-resonant conditions) is noticeably lower than that of both downstream-skewed bends (typical of super-resonant conditions) and symmetrical bends. This lower number potentially explains the lower variability of the sinuosity and the smaller number of outliers characterising upstream-skewed bends. Notably, the prevalence of super-resonant bends over sub-resonant ones agrees with the mechanistic analysis carried out by Zolezzi et al. (2009) on a dataset comprising more than 100 gravel-bed rivers.

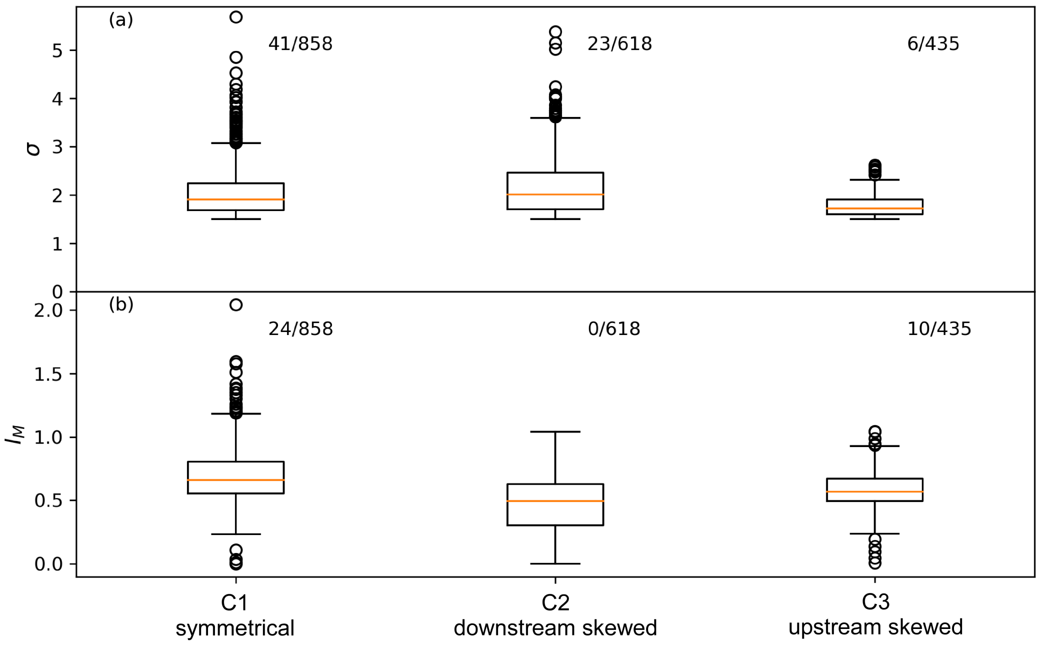

Figure 9. Box plot representation of (a) the sinuosity and (b) the Maturity Index values within each of the three clusters recognised by the automated classification procedure. The red lines indicate the median values, while the lower and upper sides of the boxes correspond to the first and third quartiles, respectively. The lower and higher horizontal segments denote the whiskers, defined as 1.5 times the interquartile range (IQR). The numbers in the upper part of the plot, indicate the the number of outliers, which are marked by empty circles, and the size of the sample.

Additional sources of complexity in interpreting the results of the automated classification are due to cutoff events, the heterogeneous composition of the floodplain, and the mutual morphodynamic influence between adjacent bends at different stages of evolution. Repeated cutoffs generally contribute to limiting the mean bend sinuosity within a given river reach, determining a continuous sequence of sinuosity fluctuations around the mean value, as shown by long-term numerical simulations (Frascati & Lanzoni, 2010). The heterogeneous composition of the floodplain may influence the intensity of these sinuosity variations (see, e.g., Figure 5c,f in Bogoni et al., 2017). The growth of a given meander bend is influenced by the evolution of the adjacent bends. In general, morphodynamic information associated with the evolution of planform waves and river bed topography propagates mainly downstream in the sub-resonant regime, while is primarily felt upstream in the super-resonant regime (Zolezzi & Seminara, 2001; Lanzoni & Seminara, 2006). The type of morphodynamic regime, in turn, depends on the hydraulic and sedimentological parameters characterising the river, as well as the mechanism dominating sediment transport (e.g. bedload in gravel-bed rivers and suspended load in sandy rivers). Finally, temporal variations in the hydrological forcing and spatial heterogeneity in the sediment composition add a further degree of difficulty in the interpretation of the statistical distribution of σ and I_M for the three classified shapes.

The potential of the automated classification procedure was tested on a highly active reach of the Ucayali River, which registered several cutoffs in the period 1984-2015 (Schwenk et al., 2017; Lopez Dubon & Lanzoni, 2019). The investigated reach is located in the Peruvian Amazon basin and has a cartesian length of about 54 km, extending approximately from Atalaya (10.7318° S, 73.7586°° W) to Pucallpa (8.3929° S, 74.5826°° W), with an average slope in the range 1-10$\times 10^{-5}$ (Santini et al., 2015). The mean annual discharge and the average maximum discharge at Pucallpa are 9720 m^3/s and 16370 m^3/s, respectively (Alvarado-Ancieta & Ettmer, 2008; Santini et al., 2015). The bed sediment has a mean size ranging from 0.17 to 0.39 mm (ECSA, 2005), with a $d_{50} \simeq 0.3$ mm at Pucallpa (Ettmer & Alvarado-Ancieta, 2010). The reach averaged channel width, estimated from satellite images, varied in the range 668-954 m (mean value 742 m) depending on the planform configuration of the river over the years. Similarly, the reach sinuosity varied between 2 and 2.6, with a mean value of 2.3. The water depth ranges between 7 m and 15 m. These variations are associated with the progressive elongation of the intrinsic river length due to meander growth and the abrupt shortening consequent to cutoffs (Figure 10a-e), and lead to continuous fluctuations in the reach average slope.

Figure 10f shows the results of the automated classification procedure throughout the considered 32 years. The investigated river reach presents predominantly symmetric bends (cluster C1) for a total of 25 years, downstream-skewed bends (cluster C2) for a total of 6 years, and a single year (1990) with prevailing upstream-skewed bend (cluster C3). The temporal distribution of the percentage of skewed bends could be interpreted as the result of the occurrence of various transitions from one morphodynamic regime to another triggered by significant cutoff events. To test this hypothesis, we computed the yearly value of the resonant value of the half-width to depth ratio β_R using the fully coupled, linearised morphodynamic model of Zolezzi and Seminara (2001). The initial (1984) planform configuration was characterised by a sinuosity of 2.12 and an average channel width of 786 m. Assuming uniform flow conditions and a plane bed (confirmed *a posteriori* by the bed classification procedure of Simons and Richardson (1966)), the average maximum discharge (16370 m^3/s) is conveyed through an equivalent rectangular cross-section with a depth of 10 m for a slope 5×10^{-5}. These conditions correspond to a half-width to depth ratio β of 39.3, a Shields stress τ_* of 1, and a dimensionless grain size d_s of 3×10^{-5}, consistent with values typically observed in sandy rivers (Francalanci et al., 2020). The resonant value of the half-width to depth ratio corresponding to this set of dimensionless parameters is $\beta_R = 29.54$. As the reach sinuosity evolves over time, the parameter values also vary accordingly. It can be easily demonstrated that (Zolezzi et al., 2009):

$$\frac{\beta}{\beta_0} = \Big[\sigma \, \frac{C_f}{C_{f0}} \Big(\frac{B_0}{B}\Big)^3\Big]^{1/3}, \qquad \frac{d_s}{d_{s0}} = \Big[\frac{1}{\sigma}\,\frac{C_{f0}}{C_f}\Big(\frac{B}{B_0}\Big)^2\Big]^{1/3}, \qquad \frac{\tau_*}{\tau_{*0}} = \frac{1}{\sigma^{2/3}}\Big(\frac{C_f}{C_{f0}}\Big(\frac{B_0}{B}\Big)^2\Big)^{1/3}. \tag{19}$$

where C_f is the friction coefficient ($C_f = [6 - 2.5\,\ln(2.5\,d_s)]^{-2}$ for plane bed conditions), and a sub-script 0 denotes the initial year.

The time series of β and β_R resulting from the analysis are shown in Figure 10h. It appears that the transition from a super-resonant dominated behaviour (epitomised by a prevalence of upstream-skewed C3 bends) to a sub-resonant dominated behaviour (embodied by a dominance of downstream-skewed C2 bends), and vice versa, is indeed plausible and is favoured by the abrupt decrease of sinuosity after big cutoffs. This is, for instance, the case of the 1992-1993 and 2004-2005 cutoffs, which likely led to a transition from a sub-resonant to a super-resonant regime. Remarkably, each passage through resonant conditions seems to enhance the formation of symmetrical C1 bends. Overall, the temporal distributions of morphodynamic regimes resulting from comparing the magnitude of β with respect to β_R and that inferred from the percentage of C2 and C3 bends is reasonable, though not perfect. This can be due to many aspects, such as the uncertainties on the hydraulic parameters adopted for the computations of β and β_R, as well as the simplifications embedded in the morphodynamic model, which consider an equivalent rectangular cross-section and does not account explicitly for suspended load effects. Moreover, deducing the dominant morphodynamic regime only from the percentages of bend classes present in the entire river

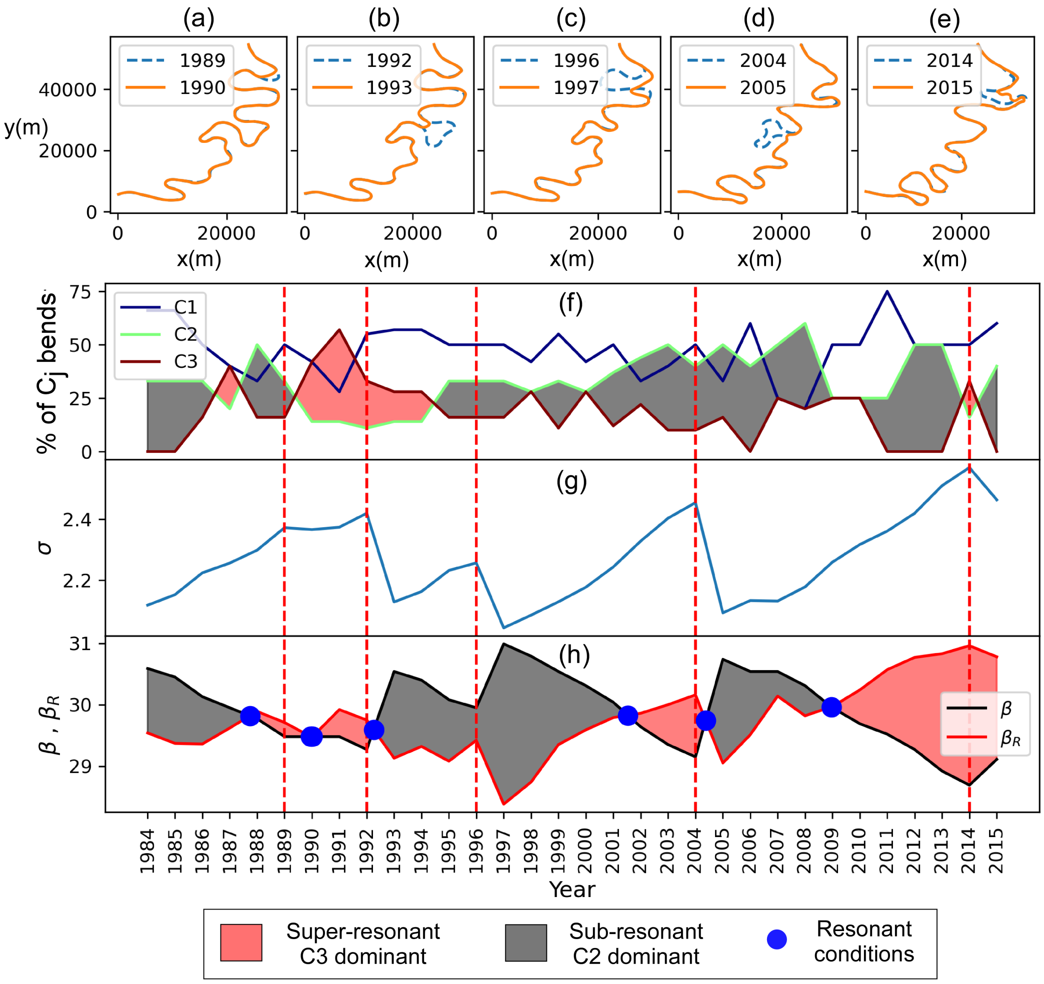

Figure 10. (a)-(e) Planforms before and after major cutoff events occurring from 1984 to 2015 along the reach of the Ucayali River comprised between Atalaya and Pucallpa. (f) The percentage of meander classes detected along the reach over various years. Temporal evolution of (f) the sinuosity distribution and (h) the values of the half-width to depth ratio, β, and the corresponding resonant value, β_R. The latter has been computed for plane bed conditions, using the total load transport formula of Engelund and Hansen (1967), and setting equal to 0.55 the coefficient accounting for gravitational effect on the transverse direction of bedload (Frascati & Lanzoni, 2013). Red dashed lines represent the cutoff events.

reach does not account for the possible inclusion of a bend in composite or multi-lobed patterns. The application of the classification procedure described above should then be regarded as a significant example of how it, in conjunction with theoretical arguments, can help to unravel the morphodynamic behaviour of a given river reach.

4.1 Limitations of the study and future work

This study proposes a data-driven classification method for single-lobe meanders, informed by the images of total energy in the wavelet spectrum of the bend curvature. This automated approach provides valuable insight for the detection and classification of single bends along a meandering river. Rather than directly analysing bend planforms, it objectively analyses the energy spectrum inherent in bend shapes without requiring the introduction of any geometric metrics, unlike previous classification approaches based on bend shape matching. The complexity of meander shapes is accounted for through the large number of parameters comprising the autoencoder architecture. The physics-based nature of the classification stems from the control exerted by bed axis curvature on migration rates, sediment transport and sorting (e.g., Güneralp & Rhoads, 2008; Finotello et al., 2018; Donovan et al., 2021). Nevertheless, some limitations of the study are worth mentioning.

The autoencoder-based classification model was trained on single-lobe bends, delimited by two consecutive inflexion points of the channel axis curvature. These bends were extracted from planforms generated synthetically using the Kinoshita curve. However, these planforms also include multiple-lobe meanders composed of various single-lobe bends. The automated procedure does not recognise these multiple-lobe shapes, and an additional, non-trivial effort is needed to include them in the classification.

The training dataset was extensive, containing $\sim 10^7$ Kinoshita-generated meanders. Despite the complex and varied shapes exhibited by real meanders, the size of this dataset could be reduced without losing the classification effectiveness. Other machine-learning classifiers need to be tested to capture the essential features of articulated meander shape features by using a smaller training dataset. This could also be particularly useful for classifying multi-lobed meanders.

The classification was based on greyscale images representing the total energy wavelet spectrum of the spatial distribution of bend curvature. For each image, the total energy was scaled according to the maximum value characterising the considered bend. This bend-specific scaling is independent of the total energy of the other bends in the dataset. The use of greyscale images simplifies the representation by limiting possible numerical values for the autoencoder, and the single scale per image preserves more features compared to normalization based on the complete dataset.

The boundaries of each cluster in Figure 6 were determined by smoothly connecting the points farthest from the centroid. Consequently, they may be sensitive to the inclusion of new data points, making it difficult to classify any point in their proximity with a high degree of confidence. This is particularly significant for clusters quite close in the latent space, as C1 and C3.

Finally, the present study is focused on single-lobe meanders, with multi-lobe meanders split into simple bends. Thus, The wavelet analysis gives information on each bend, without considering how the bends are linked. Single bends composing a multi-lobe meander are not necessarily all skewed in the same direction of the compound shape. Hence, inferring the morphodynamic regime from the prevailing percentage of single skewed (either upstream or downstream) bends must be taken with some caution. In other words, splitting composed meanders into their single bend components, as commonly done in practice, implies a loss of information in determining the morphodynamic regime based on the prevailing bend skewness.

5 Conclusions

This study developed a data-driven classification framework for meander bends based on the total energy of the wavelet spectrum of bend curvature distribution. Kinoshita-generated bends were generated, creating a large dataset. An autoencoder based on a convolutional neural network was trained and validated using this dataset. The trained neural network was then tested on remotely sensed meanders. The main findings resulting from the application of the trained neural network model are summarised below.

Investigating the energy spectrum of bend curvature through a continuous wavelet transform ensures a solid physical foundation. Curvature controls the flow field and the bed topography, ultimately correlating with meander migration, sediment transport, and grain sorting.

The autoencoder successfully transferred knowledge from Kinoshita-generated bends to real data, resulting in low binary cross-entropy loss (0.1578) for real meander. This value is quite close to the loss (0.1333) achieved for the independent Kinoshita-generated dataset used for validation.

The unsupervised classification model identified three main categories of meandering river bends: symmetric, downstream-skewed, and upstream-skewed. Applying this method to the real meander data set extracted from satellite images revealed that the symmetric single-bend meander shape is the most predominant.

An application of the classification method to a reach of the Ucayali River highlighted how the planform dynamics over a span of 32 years, from 1984 to 2015, may produce a shift in the dominant bend class. The shortening of the reach due to the cutoffs may, in fact, lead to a transition from super-critical to sub-critical conditions (or vice versa), resulting in a shift from dominant downstream-skewed bends to upstream-skewed bends (or vice versa).

In summary, this study introduced a novel framework for classifying single-lobe meander bends based on the total energy in the wavelet energy spectrum of bend curvature. This classification tool aids in identifying patterns in meander evolution, thereby potentially enhancing the effectiveness of river management interventions. A logical next step for improvement lies in extending the methodology to handle compound and multiple-lobe meanders.

Data Availability Statement

Remotely-sensed meanders were taken from datasets reported in Sylvester et al. (2019) (`https://github.com/zsylvester/curvaturepy`) and Lopez Dubon and Lanzoni (2019) (`https://zenodo.org/record/1467638\#.W83q-UvHxPY`). The link to the repository for the trained classification model is about to be created.

Author contributions

The authors contributed equally to the paper.

Competing interests

The authors declare that they have no conflict of interest.

Acknowledgments

S.L.D. acknowledges the support from the European Union Horizon 2020 research and innovation programme under the Marie Sklodowska-Curie grant agreement No. 801215 and the University of Edinburgh Data-Driven Innovation programme, part of the Edinburgh and South East Scotland City Region Deal. S.L. acknowledges the use of the AI tool "ChatGPT" (chat.openai.com) to check the English.

References

Abadi, M., Agarwal, A., Barham, P., Brevdo, E., Chen, Z., Citro, C., ... Zheng, X. (2015). *TensorFlow: Large-scale machine learning on heterogeneous systems.* Retrieved from https://www.tensorflow.org/ (Software available from tensorflow.org)

Addison, P. S. (2018). Introduction to redundancy rules: the continuous wavelet transform comes of age. *Philosophical Transaction of the Royal Society A*, *376*(20170258), 1–15. doi: 10.1098/rsta.2017.0258

Alvarado-Ancieta, C., & Ettmer, B. (2008). Morfología fluvial y erosión en curvas abruptas del Río Ucayali, Perú. *Revista de Interdisciplinaria de Cienca y Tecnología del Agua, Ingeniería Hidráulica en méxico*, *XXIII*(6), 69–90. (ISSN-0186-4076)

Antoine, J.-P., Murenzi, R., Vandergheynst, P., & Ali, S. T. (2004). Warm-up: the 1-D continuous wavelet transform. In *Two-dimensional wavelets and their relatives* (p. 1-31). Cambridge University Press. doi: 10.1017/CBO9780511543395.002

Bellizia, E., Tognin, D., Boaga, J., Cassiani, G., Leardi, R., Finotello, A., ... Ghinassi, M. (2022). From electromagnetic to sediment textural maps: an integrated approach to unravel the intra-point-bar variability of sediment properties. *Journal of the Geological Society*, *179*(4), 1–12. doi: 10.1144/jgs2021-156

Blondeaux, P., & Seminara, G. (1985). A unified bar-bend theory of river meanders. *Journal of Fluid Mechanics*, *157*, 449–470. doi: 10.1017/S0022112085002440

Bogoni, M., Putti, M., & Lanzoni, S. (2017). Modeling meander morphodynamics over self-formed heterogeneous floodplains. *Water Resources Research*, *53*(6), 5137–5157. doi: 10.1002/2017WR0207266

Bolla Pittaluga, M., & Seminara, G. (2011). Nonlinearity and unsteadiness in river meandering: A review of progress in theory and modelling. *Water Resources Research*, *38*(20), 20–38. doi: 10.1002/esp.2089

Bozzolan, E., Brenna, A., Surian, N., Carbonneau, P., & Bizzi, S. (2023). Quantifying the Impact of Spatiotemporal Resolution on the Interpretation of Fluvial Geomorphic Feature Dynamics From Sentinel 2 Imagery: An Application on a Braided River Reach in Northern Italy. *Water Resources Research*, *59*(12), 1–15. doi: 10.1029/2023WR034699

Brice, C. J. (1973). Meandering Pattern of the White River in Indiana: an Analysis. In M. Morisawa (Ed.), *Fluvial Geomorphology* (pp. 178–200). State University of New York.

Brice, C. J. (1974). Evolution of meander loops. *Geological Society of America Bulletin*, *85*(4), 581–586. doi: 10.1130/0016-7606(1974)85⟨581:EOML⟩2.0.CO;2

Brunton, S. L., & Kutz, J. N. (2019). Machine learning and data analysis. In *Data-Driven Science and Engineering: Machine Learning, Dynamical Systems, and Control* (pp. 115–116). Cambridge University Press. doi: 10.1017/9781108380690

Buffington, J. M., & Montgomery, D. R. (2013). Geomorphic classification of rivers. In J. Shroder & E. Wohl (Eds.), *Treatise on Geomorphologyy* (Vol. 9, pp. 730–767). Academic Press, San Diego, CA. doi: 10.1016/B978-0-12-374739-6.00263-3

Camporeale, C., Perona, P., Porporato, A., & Ridolfi, L. (2005). On the long-term behavior of meandering rivers. *Water Resources Research*, *41*(12), 1–13. doi: 10.1029/2005WR004109

Camporeale, C., Perona, P., Porporato, A., & Ridolfi, L. (2008). Significance of cutoff in meandering rivers dynamics. *Journal of Geophysical Research*, *113*(F1), 1–11. doi: 10.1029/2006JF000694

Camporeale, C., Perucca, E., Ridolfi, L., & Gurnell, A. M. (2013). Modeling the interactions between river morphodynamics and riparian vegetaion. *Reviews of Geophysics*, *51*(3), 379–414. doi: 10.1002/rog.20014

Chadebec, C., & Allassonniere, S. (2022). A geometric perspective on variational autoencoders. In S. Koyejo, S. Mohamed, A. Agarwal, D. Belgrave, K. Cho, & A. Oh (Eds.), *Advances in neural information processing systems* (Vol. 35, pp. 19618–19630). Curran Associates, Inc. Retrieved from `https://proceedings.neurips.cc/paper_files/paper/2022/file/7bf1dc45f850b8ae1b5a1dd4f475f8b6-Paper-Conference.pdf`

Creswell, A., Arulkumaran, K., & Bharath, A. A. (2017). *On denoising autoencoders trained to minimise binary cross-entropy.*

Crosato, A. (1990). *Simulation of meandering river processes* (Communication on Hydraulic and Geotechnical Engineering, Report 90-3). Delft (NL): Delft University of Technology.

Donovan, M., Belmont, P., & Sylvester, Z. (2021). Evaluating the relationship between meander-bend curvature, sediment supply, and migration rates. *Journal of Geophysical Research: Earth Surface*, *126*(3), 1–20. doi: 10.1029/2020JF006058

ECSA, H. (2005). *Estudio de la navegabilidad del Río ucayali en el tramo comprendido entre pucallpa y la confluencia con el Río Marañon.* Dirección general de transporte acuático, Ministerio de Transportes y Comunicaciones, Lima, (PE).

Engelund, F., & Hansen, E. (1967). *A monograph on sediment transport in alluvial streams.*

Ettmer, B., & Alvarado-Ancieta, C. A. (2010). Morphological development of the Ucayali River, Peru without human impacts. *Waldökologie, Landschaftsforschung und Naturschutz*, *10*, 77–84.

Finotello, A., D'Alpaos, M., A. Bogoni, Ghinassi, M., & Lanzoni, S. (2020). Remotely-sensed planform morphologies reveal fluvial and tidal nature of meandering channels. *Scientific reports*, *10*(54), 1–13. doi: 10.1038/s41598-019-56992-w

Finotello, A., Lanzoni, S., Ghinassi, M., Marani, M., Rinaldo, A., & D'Alpaos, A. (2018). Field migration rates of tidal meanders recapitulate fluvial morphodynamics. *Proceedings of the National Academy of Sciences*, *115*(7), 1463–1468. doi: 10.1073/pnas.171133011

Foufoula-Georgiou, E., & Kumar, P. (Eds.). (1994). *Wavelets in geophysics* (Vol. 4). AcademicPress.

Francalanci, S., Lanzoni, S., Solari, L., & Papanicolaou, A. N. (2020). Equilibrium cross section of river channels with cohesive erodible banks. *Journal of Geophysical Research: Earth Surface*, *125*, 1-20. doi: 10.1029/2019JF005286

Frascati, A., & Lanzoni, S. (2009). Morphodynamic regime and long-term evolution of meandering rivers. *Journal of Geophysical Research*, *114*(F2), 1–12. doi: 10.1029/2008JF001101

Frascati, A., & Lanzoni, S. (2010). Long-term river meandering as a part of chaotic dynamics? A contribution from mathematical modelling. *Earth Surface Processes and Landforms*, *35*(7), 791–802. doi: 10.1002/esp.1974

Frascati, A., & Lanzoni, S. (2013). A mathematical model for meandering rivers with varying width. *Journal of Geophysical Research: Earth Surface*, *118*(3), 1641–1657. doi: 10.1002/jgrf.20084

Gavrikov, P. (2020). *visualkeras.* `https://github.com/paulgavrikov/visualkeras`. GitHub.

Goodfellow, I., Bengio, Y., & Courville, A. (2016). *Deep learning.* MIT Press. Retrieved from `http://www.deeplearningbook.org`

Güneralp, I., Abad, J. D., Zolezzi, G., & Hooke, J. M. (2012). Advances and challenges in meandering channels research. *Geomorphology*, *163-164*, 1–9. doi: 10.1016/j.geomorph.2012.04.011

Güneralp, I., & Rhoads, B. L. (2008). Continuous characterization of the planform geometry and curvature of meandering rivers: Planform geometry and curvature of meandering rivers. *Geographical Analysis*, *40*, 1–25. doi: 10.1111/j.0016-7363.2007.00711.x

Guo, X., Chen, D., & Parker, G. (2019). Flow directionality of pristine meandering rivers is embedded in the skewing of high-amplitude bends and neck cutoffs. *Proceedings of the National Academy of Sciences*, *116*(47), 23448–23454. doi: 10.1073/pnas.1910874116

Gutierrez, R. R., & Abad, J. D. (2014). On the analysis of the medium term planform dynamics of meandering rivers. *Water Resources Research*, *50*(5), 3714–3733. doi: 10.1002/2012WR013358

Harris, C. R., Millman, K. J., van der Walt, S. J., Gommers, R., Virtanen, P., Cournapeau, D., . . . Oliphant, T. E. (2020). Array programming with NumPy. *Nature*, *585*(7825), 357–362.

Hickin, E. J., & Nanson, G. C. (1984). Lateral Migration Rates of River Bends. *Journal of Hydraulic Engineering*, *110*(11), 1557–1567. doi: 10.1061/(ASCE)0733-9429(1984)110:11(1557)

Hooke, J. M. (1977). The distribution and nature of changes in river channel pattern. In K. J. Gregory (Ed.), *River channel changes* (pp. 265–280). Wiley-Blackwell, Chichester (UK). (ISBN:978-0471995241)

Hooke, J. M. (2013). River meandering. In E. Wohl & J. F. Shroder (Eds.), *Treatise on geomorphologyy* (Vol. 9, pp. 260–288). Academic Press, San Diego, CA. doi: 10.1016/B978-0-12-374739-6.00241-4

Hooke, J. M., & Harvey, A. M. (1983). Meander changes in relation to bend morphology and secondary flows. In J. D. Collinson & J. J. Lewin (Eds.), *Modern and ancient fluvial systems* (Vol. 6, pp. 121–132). Wiley-Blackwell, Oxford (UK). doi: 10.1002/9781444303773.ch9

Howard, A. D., & Hemberger, A. T. (1991). Multivariate characterization of meandering. *Geomorphology*, *4*(3–4), 161–186. doi: 10.1016/0169-555X(91)90002-R

Howard, A. D., & Knutson, T. R. (1984). Sufficient conditions for river meandering: a simulation approach. *Water Resources Research*, *20*(11), 1659–1667. doi: 10.1029/WR020i011p01659

Ielpi, A., & Ghinassi, M. (2014). Planform architecture, stratigraphic signature and morphodynamics of an exhumed Jurassic meander plain (Scalby Formation, Yorkshire, UK). *Sedimentology*, *61*(7), 1923–1960. doi: 10.1111/sed.12122

Ielpi, A., Lapôtre, M. G. A., Gibling, M. R., & Boyce, C. K. (2022). The impact of vegetation on meandering rivers. *Nature Reviews Earth & Environment*, *3*, 165–178. doi: 10.1038/s43017-021-00249-6

Ikeda, S., Parker, G., & Sawai, K. (1981). Bend theory of river meanders. Part 1. Linear development. *Journal of Fluid Mechanics*, *112*, 363–377. doi: 10.1017/S0022112081000451

Kingma, D. P., & Welling, M. (2022). Auto-encoding variational bayes. *arXiv e-prints*, 12–14. doi: 10.48550/arXiv.1312.6114

Kinoshita, R. (1961). *Investigation of channel deformation in Ishikari river* (Hydraulic laboratory report, hyd no. 325). Tokyo (JPN): Natural Resources Division, Ministry of Science and Technology of Japan.

Kleinhans, M. G., McMahon, W. J., & Davies, N. (2023). What even is a meandering river? A philosophy-enhanced synthesis of multi-level causes and systemic interactions contributing to river meandering. In A. Finotello, P. Durkin, & Z. Sylvester (Eds.), *Meandering Streamflows: Patterns and Processes across Landscapes and Scales* (Vol. 540, pp. 1–52). Wiley-Blackwell, Hoboken (US). doi: 10.1144/SP540-2022-138

Kriegel, H. P., Schubert, E., & Zimek, A. (2017, 8). The (black) art of runtime evaluation: Are we comparing algorithms or implementations? *Knowledge and Information Systems*, *52*, 341-378. doi: 10.1007/s10115-016-1004-2

Lagasse, P. F., Spitz, W. J., Zevenbergen, L. W., & Zachmann, D. W. (2004). *Handbook for predicting stream meander migration.* Washington, D.C. (US): National Cooperative Highway Research Program, report 533. (ISBN: 0-309-088143)

Langbein, W. B., & Leopold, L. B. (1966). *River meanders - Theory of minimum variance* (Professional Paper 422-H). Washington, D.C. (US): U.S. Geological Survey. doi: 10.3133/pp422H

Langendoen, E. J., Mendoza, A., Abad, J. D., Tassi, P., Wang, D., Ata, R., . . . Hervouet, J.-M. (2016). Improved numerical modeling of morphodynamics of rivers with steep banks. *Advances in Water Resources*, *93*, 4–14. doi: 10.1016/j.advwatres.2015.04.002

Lanzoni, S. (2022). Morphodynamic Modeling of Alluvial Rivers and Floodplains. In

J. F. Shroder (Ed.), *Reference Module in Earth Systems and Environmental Sciences* (Vol. 10, pp. 83–109). Elsevier. doi: 10.1016/B978-0-12-818234-5.00154-1

Lanzoni, S., & Seminara, G. (2006). On the nature of meander instability. *Journal of Geophysical Research*, *111*, 1–14. doi: 10.1029/2005JF000416

Lazarus, E. D., & Constantine, J. A. (2013). Generic theory for channel sinuosity. *Proceedings of the National Academy of Sciences of the United States of America*, *110*(21), 8447–8452. doi: 10.1073/pnas.1214074110

Lee, G., Gommers, R., Waselewski, F., Wohlfahrt, K., & O'Leary, A. (2019, 4). Pywavelets: A python package for wavelet analysis. *Journal of Open Source Software*, *4*, 1237. doi: 10.21105/JOSS.01237

Leopold, L. B., & Wolman, M. G. (1957). *River channel patterns: Braided, meandering, and straight.* U.S. Government Printing Office. Retrieved from https://books.google.co.uk/books?id=kUMWcgAACAAJ

Leopold, L. B., Wolman, M. G., & Miller, J. P. (1964). *Fluvial processes in geomorphology.* San Francisco (US): Freeman. (ISBN: 978-0486685885)

Leuven, J. R. F. W., van Maanen, B., Lexmond, B. R., van der Hoek, B. V., Spruijt, M. J., & Kleinhans, M. G. (2018). Dimensions of fluvial-tidal meanders: Are they disproportionally large? *Geology*, *46*(10), 923–926. doi: 10.1130/G45144.1

Lopez Dubon, S., & Lanzoni, S. (2019). Meandering evolution and width variations: A physics-statistics-based modeling approach. *Water Resources Research*, *55*(1), 76–94. doi: 10.1029/2018WR023639

Mosselman, E. (1998). Morphological modelling of rivers with erodible banks. *Hydrological Processes*, *12*(8), 1357-1370. doi: 10.1002/(SICI)1099-1085(19980630)12:81357::AID-HYP6193.0.CO;2-7

Motta, D., Abad, J. D., Langendoen, E. J., & GarcÃa, M. H. (2012). The effects of floodplain soil heterogeneity on meander planform shape. *Water Resources Research*, *48*(9), 1–17. doi: 10.1029/2011WR011601

Nanson, G. C., & Hickin, E. J. (1983). Channel Migration and Incision on the Beatton River. *Journal of Hydraulic Engineering*, *109*(3), 327–337. doi: 10.1061/(ASCE)0733-9429(1983)109:3(327)

Parker, G., Shimizu, Y., Wilkerson, G. V., Eke, E. C., Abad, J. D., Lauer, J. W., … Voller, V. R. (2011). A new framework for modeling the migration of meandering rivers. *Earth Surface Processes and Landforms*, *36*(1), 70–86. doi: 10.1002/esp.2113

Pedregosa, F., Varoquaux, G., Gramfort, A., Michel, V., Thirion, B., Grisel, O., … Duchesnay, E. (2011). Scikit-learn: Machine learning in Python. *Journal of Machine Learning Research*, *12*, 2825–2830. doi: 10.48550/arXiv.1201.0490

Ran, Y., Liu, Y., Wu, S., Li, W., Zhu, K., Ji, Y., … Huang, P. (2022). A higher river sinuosity increased riparian soil structural stability on the downstream of a dammed river. *Science of The Total Environment*, *802*, 1–10. doi: 10.1016/j.scitotenv.2021.149886

Repasch, M., Scheingross, J. S., Hovius, N., Lupker, M., Wittmann, H., Haghipour, N., … Sachse, D. (2021). Fluvial organic carbon cycling regulated by sediment transit time and mineral protection. *Nature Geoscience*, *14*, 842–848. doi: 10.1038/s41561-021-00845-7

Rosgen, D. L. (1994). A Classification of Natural Rivers. *Catena*, *22*(3), 169–199. doi: 10.1016/0341-8162(94)90001-9

Ruby, U. A., Theerthagiri, P., Jacob, I. J., & Vamsidhar, Y. (2020, 8). Binary cross entropy with deep learning technique for image classification. *International Journal of Advanced Trends in Computer Science and Engineering*, *9*, 5393-5397. doi: 10.30534/ijatcse/2020/175942020

Russell, C. E., Mountney, N. P., Hodgson, D. M., & Colombera, L. (2018). A novel approach for prediction of lithological heterogeneity in fluvial point-bar deposits from analysis of meander morphology and scroll-bar pattern. In M. Ghinassi, L. Colombera, N. P. Mountney, A. J. H. Reesink, & M. Bateman (Eds.), *Fluvial Meanders and Their Sedimentary Products in the Rock Record* (Vol. 48, pp. 385–418). Wiley-Blackwell.

doi: 10.1002/9781119424437.ch15

Santini, W., Martinez, J.-M., Espinoza-Villar, R., Cochonneau, G., Vauchel, P., Moquet, J.-S., … Guyot, J.-L. (2015, 11-14 December). Sediment budget in the Ucayali River basin, an Andean tributary of the Amazon River. In *Proceedings of the International Association of Hydrological Sciences 2014 - Sediment Dynamics from the Summit to the Sea* (Vol. 367, pp. 320–325). New Orleans, Louisiana (USA). doi: 10.5194/piahs-367-320-2015

Savitzky, A., & Golay, M. J. E. (1964). Smoothing and Differentiation of Data by Simplified Least Squares Procedures. *Analytical Chemistry*, *36*(8), 1627–1639. doi: 10.1021/ac60214a047

Schumm, S. A. (1985). Patterns of alluvial rivers. *Annual Review of Earth and Planetary Sciences*, *13*, 5–27. doi: 10.1146/annurev.ea.13.050185.000253

Schwenk, J., & Foufoula-Georgiou, E. (2016). Meander cutoffs nonlocally accelerate upstream and downstream migration and channel widening. *Geophysical Research Letters*, *43*, 12437–12445. doi: 10.1002/2016GL071670

Schwenk, J., Khandelwal, A., Fratkin, M., Kumar, V., & Foufoula-Georgiou, E. (2017). High spatiotemporal resolution of river planform dynamics from landsat: The RivMAP toolbox and results from the Ucayali River. *Earth and Space Science*, *4*(2), 46–75. doi: 10.1002/2016EA000196

Schwenk, J., Lanzoni, S., & Foufoula-Georgiou, E. (2015). The life of a meander bend: Connectingshape and dynamics via analysis of anumerical model. *Journal Geophysical Research: Earth Surface*, *120*, 690–710. doi: 10.1002/2014JF003252

Seminara, G., Lanzoni, S., & Tambroni, N. (2023). *Theoretical morphodynamics: River meandering.* Florence University Press, Florence.

Seminara, G., & Tubino, M. (1992). Weakly nonlinear-theory of regular meanders. *Journal of Fluid Mechanics*, *244*, 257-288. doi: 10.1017/S0022112092003069

Seminara, G., Zolezzi, G., Tubino, M., & Zardi, D. (2001). Downstream and upstream influence in river meandering. part 2. planimetric development. *Journal of Fluid Mechanics*, *438*, 213–230. doi: 10.1017/S0022112001004281

Sgarabotto, A., Bellizia, E., Finotello, A., D'Alpaos, A., Lanzoni, S., Boaga, J., … Ghinassi, M. (2024). Reconstructing sediment distribution in meandering river deposits through a simplified numerical modelling approach, with applications to the Holocene deposits of the Venetian Plain (Italy). In A. Finotello, P. R. Durkin, & Z. Sylvester (Eds.), *Meandering Streamflows: Patterns and Processes across Landscapes and Scales* (Vol. 540, pp. 1–21). London: The Geological Society of London. doi: 10.1144/SP540-2022-220

Simons, D. B., & Richardson, E. V. (1966). *Resistance to Flow in Alluvial Channels* (Geological Survey Professional, Paper 422J). Washington D.C. (US): US Government Printing Office.

Sun, X., Shiono, K., Rameshwaran, P., & Chandler, J. H. (2010). Modelling vegetation effects in irregular meandering river. *Journal of Hydraulic Research*, *48*(6), 775-783. doi: 10.1080/00221686.2010.531101

Sylvester, Z., Durkin, P. R., & Covault, J. A. (2019). High curvatures drive river meandering. *Geology*, *47*(10), 263–266. doi: 10.1130/G45608.1

Tary, J. B., Herrera, R. H., & van der Baan, M. (2018). Analysis of time-varying signals using continuous wavelet and synchro squeezed transforms. *Philosophical Transaction of the Royal Society A*, *376*(20170254), 1–16. doi: 10.1098/rsta.2017.0254

Tschannen, M., Bachem, O., & Lucic, M. (2018). Recent advances in autoencoder-based representation learning. *Computing Research Repository*, *abs/1812.05069*. doi: 10.48550/arXiv.1812.05069

van der Walt, S., Schönberger, J. L., Nunez-Iglesias, J., Boulogne, F., Warner, J. D., Yager, N., … Yu, T. (2014). scikit-image: image processing in Python. *PeerJ*, *2*, 1–18. doi: 10.7717/peerj.453

Vermeulen, B., Hoitink, A. J. F., Zolezzi, G., Abad, J. D., & Aalto, R. (2016). Multiscale structure of meanders. *Geophysical Research Letters*, *43*(7), 3288–3297. doi: 10.1002/2016GL0682387

Weisscher, S. A. H., Shimizu, Y., & Kleinhans, M. G. (2019). Upstream perturbation and floodplain formation effects on chute-cutoff-dominated meandering river pattern and dynamics. *Earth Surface Processes and Landforms*, *44*(11), 2156–2169. doi: 10.1002/esp.4638

Wohl, E., Lane, S. N., & Wilcox, A. C. (2015). The science and practice of river restoration. *Water Resources Research*, *51*(8), 5974–5997. doi: 10.1002/2014WR016874

Wu, F.-C., Shao, Y.-C., & Chen, Y.-C. (2011). Quantifying the forcing effect of channel width variations on free bars: morphodynamic modelling based on characteristic dissipative Galerkin scheme. *Journal of Geophysics Research*, *116*(F3), 1–20. doi: 10.1029/2010JF001941

Yan, N., Colombera, L., & Mountney, N. P. (2021). Controls on fluvial meander-belt thickness and sand distribution: Insights from forward stratigraphic modelling. *Sedimentology*, *68*(5), 1831–1860. doi: 10.1111/sed.12830

Zolezzi, G., & Güneralp, I. (2015). Continuous wavelet characterization of the wavelengths and regularity of meandering rivers. *Geomorphology*, *252*, 98–111. doi: 10.1016/j.geomorph.2015.07.029

Zolezzi, G., Luchi, R., & Tubino, M. (2009). Morphodynamic regime of gravel bed, single-thread meandering rivers. *Journal of Geophysical Research: Earth Surface*, *114*, 1–14. doi: 10.1029/2007JF000968

Zolezzi, G., Luchi, R., & Tubino, M. (2012). Modelling morphodynamic processes in meandering rivers with spatial width variations. *Review Geophysics*, *50*(4), 1–24. doi: 10.1029/2012RG000392

Zolezzi, G., & Seminara, G. (2001). Downstream and upstream influence in river meandering. Part 1. General theory and application to overdeepening. *Journal of Fluid Mechanics*, *438*, 213–230. doi: 10.1017/S0022112001004281

A Curvature-Based Framework for Automated Classification of Meander Bends

Sergio Lopez Dubon[1], Alessandro Sgarabotto[2,3], and Stefano Lanzoni[4]

[1]School of Engineering, University of Edinburgh, Edinburgh, United Kingdom
[2]School of Geography, Earth and Environmental Sciences, University of Plymouth, Plymouth, United Kingdom
[3]School of Engineering, University of Birmingham, Birmingham, United Kingdom
[4]Department of Civil, Environmental and Architectural Engineering, University of Padova, Padova, Italy

Key Points:

- A curvature-based classification framework of meander bends was successfully trained over Kinoshita-generated meanders.
- By testing the trained framework over real meander bends, 3 classes were found, namely symmetrical, downstream-skewed, and upstream-skewed.
- The proposed framework detects the dominant shape class in river reaches and how this changes over time when cutoff events occur.

Corresponding author: Sergio Lopez Dubon, `Sergio.LDubon@ed.ac.uk`

Abstract

River meanders are one of the most recurrent and varied patterns in fluvial systems. Multiple attempts have been made to detect and categorise patterns in meandering rivers to understand their shape and evolution. A novel data-driven approach was used to classify single-bend meanders. A dataset containing approximately 10 million single-lobe meander bends was generated using the Kinoshita curve. A neural network autoencoder was trained over the curvature energy spectra of Kinoshita-generated meanders. Then, the trained network was then tested on real meander bends extracted from satellite images, and the energy spectrum in the meander curvature was reconstructed accurately thanks to the autoencoder architecture. The meander spectrum reconstruction was clustered, and three main bend shapes were found associated with the meander datasets, namely symmetric, upstream-skewed, and downstream-skewed. The autoencoder-based classification framework allowed bend shape detection along rivers, finding the dominant pattern with implications on migration trends. By studying the shift in the prevailing bend shape over time, cutoff events were approximately forecast along the Ucayali River, whose migration was remotely sensed for 32 years. Overall, the method proposed opens the venue to data-driven classifications to understand and manage meandering rivers. Bend shape classification can thus inform restoration and flood control practices and contribute to predicting meander evolution from satellite images or sedimentary records. **Keywords**: Meandering rivers; Automatic Classification; Wavelets; Model Transferability; Autoencoder; Pattern recognition

Plain Language Summary

Single-thread rivers commonly cut through alluvial floodplains with continuous sinuous curves. Classifying meanders provides a key to understanding their shape and, thus, learning how they have changed over time. A novel classification framework was proposed using a machine-learning model for pattern recognition in images. This model was trained over the curvature energy distribution within the meander bends generated from analytical relations. The classification framework was then tested over a set of real meander bends extracted from satellite images. The trained model grasped the most important features contained in curvature energy distribution, grouping the meander data set into three bend-shaped clusters, namely symmetric, upstream-skewed, and downstream-skewed. The proposed framework was then used to find the predominant bend class and its shifts during river migration, offering a different perspective on meander evolution. Bend shape classification can be used to guide restoration and flood control plans and predict meandering trends from satellite images or sedimentary records.

1 Introduction

Meander bends are patterns widespread in both fluvial and tidal systems (e.g., Leopold et al., 1964; Leuven et al., 2018; Finotello et al., 2020). While migrating on the alluvial plain, meander bends evolve by growing in amplitude, fattening, and skewing. Eventually, the sinuous loops, if too narrow, cut off starting a new course (e.g., Kleinhans et al., 2023).

Restoration practices often include re-introducing meanders to enhance biodiversity and mitigate flood peaks by promoting floodplain inundation and slowing down the flow (e.g., Wohl et al., 2015). River sinuosity associated with the presence of meanders favours the accommodation of organic matter, improving the stability of the riparian soil and reducing the impact of dam constructions (Ran et al., 2022). Moreover, meandering rivers, especially those migrating actively on floodplains, are more efficient in carbon sequestration than straight rivers, thus contributing to climate change mitigation (Repasch et al., 2021). Studies on static planform shapes and their classification can also improve our understanding of meander dynamics and give insights on paleochannels (e.g., Yan et al., 2021; Bellizia et al., 2022; Sgarabotto et al., 2024). Overall, the study of meander morphology can help to understand how meandering rivers evolve and provide insights for effective river management.

Bend geometries can be very complex. They include single-lobe bends and multi-lobe bends when adjacent bends merge, making it hard to detect the single-bends inflexion points and apexes unambiguously. Different classification frameworks have been proposed to address the complexity and variety of meandering patterns and help the understanding of their morphodynamics (Leopold et al., 1964; Howard & Hemberger, 1991; Lagasse et al., 2004; Güneralp et al., 2012; Lanzoni, 2022). Classifications serve various purposes, and their relevance depends on the ease of use, the possibility to analyse many different patterns, the ability to grasp the physical processes, and, more recently, the potential for automation (Buffington & Montgomery, 2013). In general, meander classifications can be grouped into qualitative approaches, based on shape matching, and quantitative approaches, which rely on bend parametrisation, bend evolution frameworks, spectral methods, or data-driven methods (Hooke, 2013).

The visual similarity between bends led to a classification in which the observed meanders are subjectively matched to shape prototypes (Brice, 1974; Ielpi & Ghinassi, 2014). To encompass even complex morphologies, the number of classes is progressively increased. For example, the four classes initially proposed by Brice (1973), were extended to 16 by Brice (1974) and further expanded to 70 by Hooke (1977). A simplification of this approach was put forward by Hooke and Harvey (1983), who, in addition to the shape matching, considered various simple mechanisms to account for evolution processes, such as free and confined mender migration, bend growth, lobbying, double heading, formation of new bends, cutoff, and retraction. The subjective nature of visual classification was later supported by objective shape assessments based on ensemble statistics of the planforms included between successive inflexion points of the channel axis. The bend shape was investigated by analysing geometrical features such as the radius of curvature, the cartesian and intrinsic lengths, the sinuosity, and the asymmetry index. Bend shapes were initially classified using single metrics, such as the sinuosity (Schumm, 1985) and the radius of curvature (Nanson & Hickin, 1983; Hickin & Nanson, 1984). Subsequently, shape characterisation was improved by considering multiple metrics. Slope, sinuosity, and width-to-depth ratio were used by Rosgen (1994) to characterise river systems. More recently, Russell et al. (2018) proposed to use a polygon built around a meander bend such that its sides were tangent to the meander centreline. The length of the meander centreline was normalised with the bend width, and the ratio between the area and perimeter of the polygon concurred to define the various meander classes. Nevertheless, all the aforementioned methodologies present two main problems. First, they are too complicated to encompass as many shapes as possible. Indeed, the geometrical metrics considered insufficient to characterise unambiguous single meander bends. In contrast, a suite of them can be used for the statistical characterisation of an entire river reach (Camporeale et al., 2005; Frascati & Lanzoni, 2009). Secondly, the great variety of meander shapes (e.g., Figure 1a-d) makes the above classification frameworks cumbersome to automate and test on a large meander dataset.

To overcome the issues of shape matching and bend parametrisation approaches, the bend evolution was described through simplified mechanistic models aimed to reproduce the variety of meander bends (Hooke & Harvey, 1983; Lagasse et al., 2004). In particular, the explanation of meander initiation through the bend instability mechanism (Ikeda et al., 1981; Blondeaux & Seminara, 1985) led to the formulation of numerous deterministic models of meander morphodynamics. Early models described the evolution of meander bends considering a linearised treatment of the morphodynamic problem, and using a simplified bank erosion law based on the difference in flow speed experienced at the outer and inner banks (Crosato, 1990; Seminara & Tubino, 1992; Seminara et al., 2001). Further mechanisms were subsequently added in this type of models, such as the occurrence of cutoffs (Howard & Knutson, 1984; Camporeale et al., 2008; Schwenk & Foufoula-Georgiou, 2016; Weisscher et al., 2019), the effects of height and sediment composition of the banks and

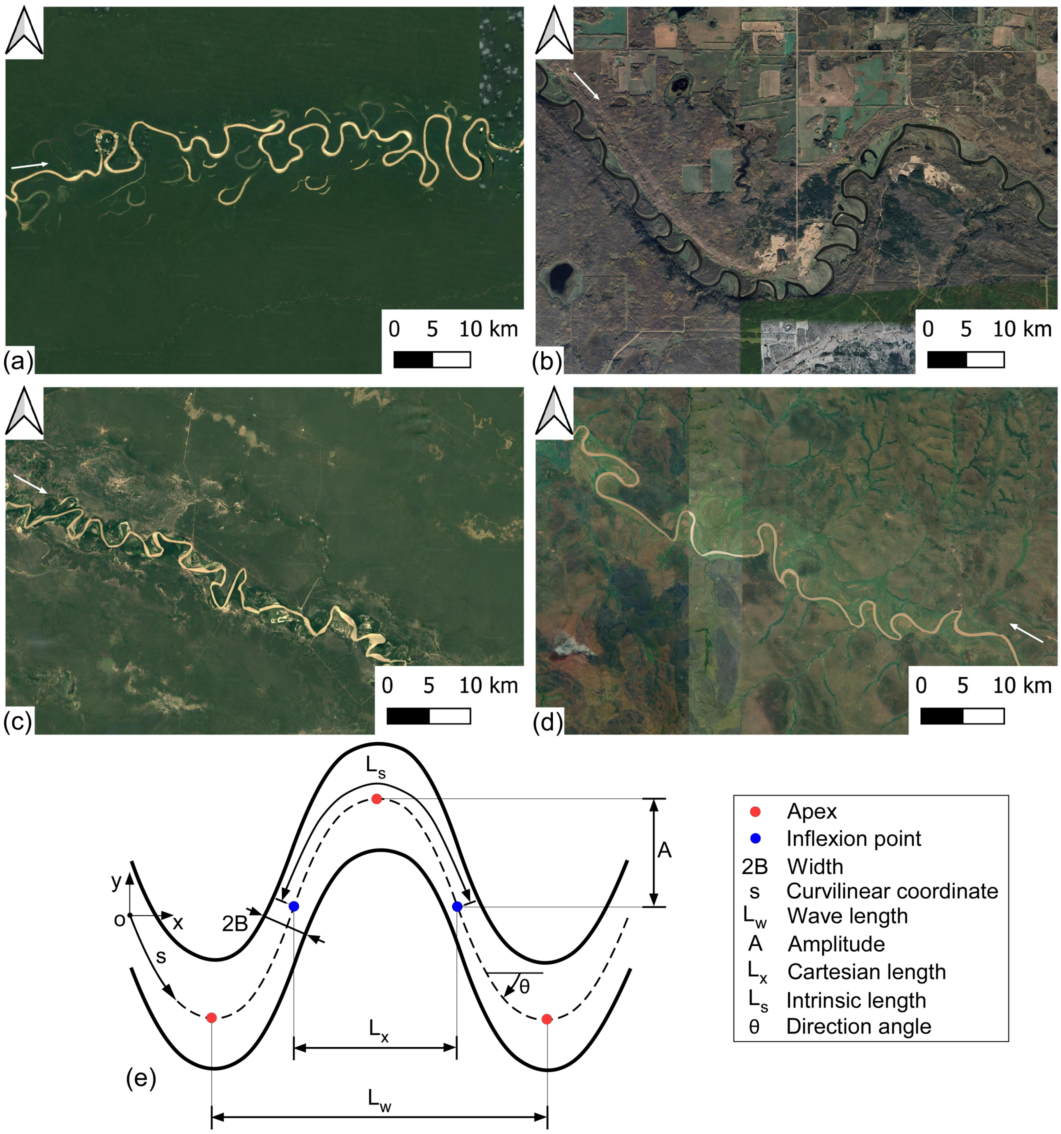

Figure 1. Satellite images of meandering patterns along the (a) Juruá (Brazil), (b) Beaver (Canada), (c) Bermejo (Argentina), and (d) Kwango (Angola/Congo) rivers. All the images were taken in May 2023: (a) and (c) were extracted from Bing Areal Maps; (b) and (d) were extracted from Google Satellite. (e) A schematic illustrating the main geometrical features of a meander bend.

the formation of slump blocks (Mosselman, 1998; Parker et al., 2011; Langendoen et al., 2016), the presence of channel width variations (Wu et al., 2011; Zolezzi et al., 2012; Frascati & Lanzoni, 2013; Lopez Dubon & Lanzoni, 2019), and the consequences of floodplain heterogeneity due to former river wanderings or geological constraints (Motta et al., 2012; Bogoni et al., 2017). If included in the modelling framework, riparian vegetation was found to reduce the shear stress distribution and affect bank erodibility, narrowing the stream and slowing down the migration process in the long-term (Sun et al., 2010; Camporeale et al., 2013; Weisscher et al., 2019; Ielpi et al., 2022). Linearised morphodynamic models were also used to characterise meander morphology in terms of the potential extension of the meander belt (Camporeale et al., 2005). Specifically, the ratio between the meander belt width and the channel width was used to define an entrenchment ratio that quantifies the overall propensity of a meandering river to migrate laterally. This metric was also used in Rosgen classification (Rosgen, 1994).

An attempt was put forward to integrate the shape characterisation with hydro-morphodynamic information by Bolla Pittaluga and Seminara (2011) and Schwenk et al. (2015). In particular, Bolla Pittaluga and Seminara (2011) proposed a mechanistic classification of meander bends relying on four dimensionless groups quantifying the relative importance of friction as compared to local inertia (Σ), longitudinal convection ($\mathfrak{L}$), centrifugal inertia (δ), and lateral convection $\mathfrak{b}$. These four parameters are defined as:

$$\Sigma = \frac{D_u}{L_{T0}\sqrt{C_{fu}}}, \quad \mathfrak{L} = \frac{D_u}{L\sqrt{C_f u}}, \quad \delta = \frac{D_u}{R_0\sqrt{C_{fu}}}; \quad \mathfrak{b} = \frac{D_u}{B\sqrt{C_{fu}}} \tag{1}$$

where D_u is the uniform flow depth, C_{fu} is the corresponding friction coefficient, B is the half-width of the channel, L_{T0} is a characteristic convective scale defined as the distance covered by a fluid particle moving with a velocity U_u in the time scale T_0, L is a characteristic spatial scale (e.g. the meander wavelength), and R_0 is an appropriate radius of curvature. The typical values of these groups were extracted from a real meanders database (Lagasse et al., 2004). Based on the values attained by the above parameters, mildly curved bends were found to be quite common. Specifically, half of the meanders analysed by Bolla Pittaluga and Seminara (2011) exhibited a relatively small value (below 0.18) of the parameter δ. Even though classifications of meander shapes relying on hydraulic parameters are not widely adopted, various studies have highlighted the strong link between meander shape morphology and its formative dynamics (e.g., Schwenk et al., 2015; Guo et al., 2019).

Meandering morphology has also been characterised through spectral analysis, considering flow direction or channel axis curvature (Howard & Hemberger, 1991). Indeed, bend curvature provides valuable insight into meander shape, given its strong influence on the flow field, sediment dynamics, and ultimately, on the rate of bend migration (Güneralp & Rhoads, 2008; Finotello et al., 2018; Donovan et al., 2021). Meandering patterns were also mimicked through a random walk process, where changes in direction were assumed as independent random variables, representing the effects of disturbances to the system (Langbein & Leopold, 1966). In addition, Langbein and Leopold (1966) argued that changes in meandering direction can be well approximated by a sine-generated curve that minimises the variance from the stable state defined by the mean downstream direction. By describing the meandering process as completely random, the meandering path degenerates into a straight line when disturbances to the system are removed. To overcome this issue, river meanders were treated as deterministic oscillations with a random component attributed to a variable floodplain composition, affecting the planform angle (Langbein & Leopold, 1966; Howard & Hemberger, 1991) or vertical bank elevation (Lazarus & Constantine, 2013). More recently, meander morphology was investigated by analysing the energy spectrum of curvature distribution in a bend by wavelets (Gutierrez & Abad, 2014; Zolezzi & Güneralp, 2015).

Despite the numerous attempts outlined above, an automatic, objective classification of meander bends has yet to be developed. Machine learning offers techniques to find patterns in large datasets, proving its versatility in many geomorphology applications, such as the detection of fluvial geomorphic features from satellite images (Bozzolan et al., 2023).

The present study proposes a physics-based, data-driven method to automatically classify meander bends, based on the energy spectrum of the curvature distribution. This approach is deemed to overcome the shortcomings of existing classification methods.

The rest of the paper is structured as follows. Section 2 presents the methodologies used to generate synthetic meander planforms and extract real meander shapes from satellite images. This section also outlines the development of the data-driven unsupervised classification framework, relying on the energy spectrum of the bend curvature distribution. Section 3 presents the classification results obtained for real meander bends. In section 4, the classification results are discussed in terms of meander morphodynamics, also considering the specific case of a reach of the Ucayali River. Finally, section 5 reports the conclusions.

2 Methods

The automated classification framework developed in this study exploits the information contained in the spatial distribution of channel axis curvature. We propose to summarise this information through its wavelet spectrum, which is then used to automatically identify the typology of a given meander bend. A neural network autoencoder was trained on the wavelet energy spectra extracted from a large series of synthetic meanders. The classification procedure based on this autoencoder was subsequently tested on an independent set of synthetically generated bends and real meander shapes extracted from satellite images.

The development of the overall framework included six steps (Figure 2). First, single-bend meanders were generated from the Kinoshita curve for both training and testing purposes. Next, the continuous wavelet transform was applied to the spatial distribution of channel axis curvature for each bend, computing the corresponding total energy wavelet spectrum. Third, the images of the energy spectra were used to train an autoencoder which compresses the information contained in each image, locates it in a latent two-dimensional space and eventually reconstructs it. This autoencoder was then tested over an independent set of synthetically generated bends, as well as on real single-bend meanders. Fifth, the K-means algorithm was used to find out the optimal number of clusters through which the real meanders can be grouped in the latent space. Finally, the cluster centroid was used to represent the characteristic shape of the cluster, regardless of bend amplitude and wavenumber. Below, we summarise the key features of the various steps.

2.1 Synthetically-generated meanders

The synthetic sets of meander planforms used first to train and subsequently to test the automatic classification procedure were generated according to the so-called Kinoshita curve (Kinoshita, 1961). This curve represents a slightly modified version of the sine-generated curve of (Langbein & Leopold, 1966), and can describe a rich spectrum of meander shapes (Seminara et al., 2001; Vermeulen et al., 2016; Seminara et al., 2023), from single-lobe meanders, which have only two inflexion points of the curvature distribution, to compound meanders, with multiple inflexion points. Denoting by s the intrinsic coordinate of the channel axis and L_w the meander wavelength (Figures 1e and 2a), the Kinoshita curve expresses the angle that the tangent to the channel axis forms with that of the valley as

$$\theta = \theta_1 \,\sin(\lambda\, s) + \theta_{3r}\,\cos(3\,\lambda\, s) + \theta_{3i}\,\sin(3\,\lambda\, s), \tag{2}$$

where $\lambda = 2\,\pi/L_w$ is the meander wavenumber. The spatial distribution of the channel axis curvature $c(s)$ is readily computed as

$$c(s) = -\frac{d\theta}{ds} = c_0\,\big[\cos(\lambda\, s) - c_F\,\sin(3\,\lambda\, s) + c_S\,\cos(3\,\lambda\, s)\big], \tag{3}$$

with $c_0 = \lambda\theta_1$, $c_F = 3\,\theta_{3r}/\theta_1$ and $c_S = 3\,\theta_{3i}/\theta_1$ dimensionless parameters controlling the bend shape. In particular, c_F is associated with the bend fattening, whereas c_S determines whether the bend is skewed upstream or downstream.

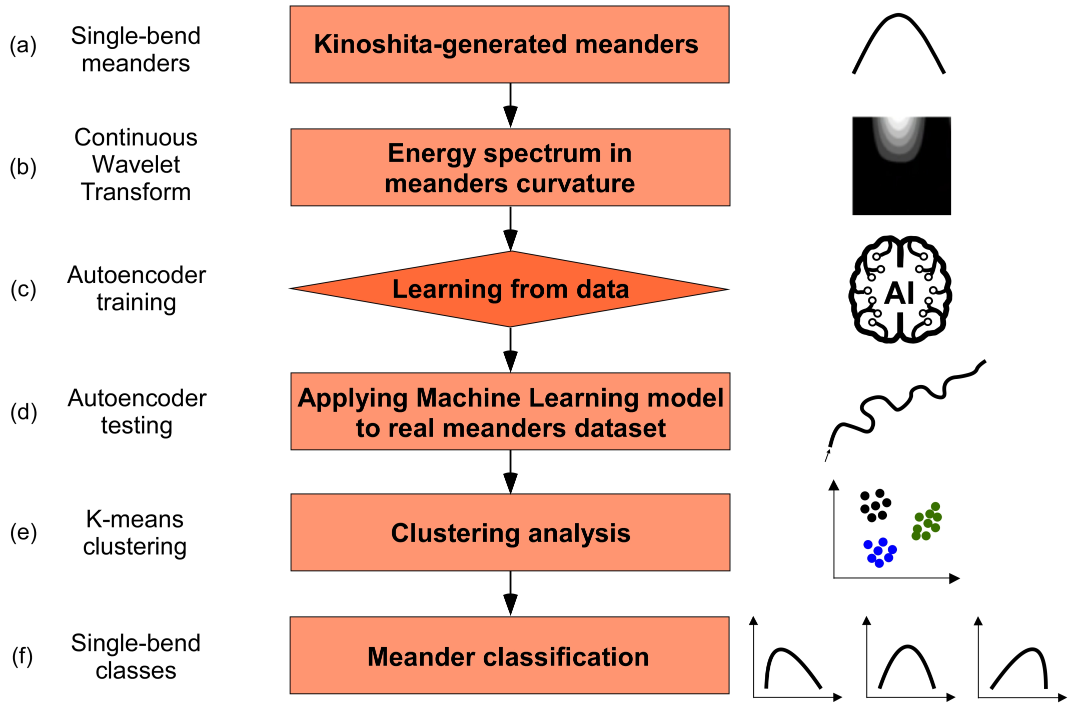

Figure 2. Flowchart illustrating the six steps involved in developing the automated classification procedure of meander bends based on the energy spectrum of the spatial distribution of channel axis curvature.

The intrinsic coordinate s and the cartesian coordinates (x, y) are related together by the transformations

$$\frac{dx}{ds} = \cos\theta(s), \qquad \frac{dy}{ds} = \sin\theta(s), \tag{4}$$

allowing to reconstruct the bend shape in the (x, y)-plane.

To produce a meaningful set of planform geometries, the values of the parameters θ_1, θ_{3r} and θ_{3i} were chosen taking advantage of the real meander dataset of Lagasse et al. (2004). A statistical analysis indicated that the wavenumber of meanders can be described by a Probability Distribution Function (PDF) based on the gamma function Γ, namely

$$f_\Gamma(\xi) = \frac{\xi^{(\gamma_a - 1)}}{\gamma_b^{\gamma_a}\,\Gamma(\gamma_a)} \exp\left[-\left(\frac{\xi}{\gamma_b}\right)\right], \tag{5}$$

where the best-fit values of the coefficients γ_a and γ_b, are equal to 12.728 and 0.0265, respectively. These values lead to a coefficient of determination R^2 equal to = 96.13%, and a Bayesian Information Criterion (BIC) of -2.551 $\cdot 10^2$.

The wavenumbers of the Kinoshita-generated meanders were selected by randomly sampling from the PDF (5). On the other hand, as no information was available about the statistical distribution of the parameters θ_1, θ_{3r} and θ_{3i}, their values were randomly sampled from a uniform PDF using a pseudo-random number generator function (Harris et al., 2020). Moreover, to avoid intertwined loops, the coefficients θ_{3r} and θ_{3i} were selected in the range $[-1, 1]$ assuming a zero mean value. Finally, the amplitude coefficient θ_1 was chosen in the range $[4/\pi - 1, 4/\pi + 1]$, with a mean value equal to $4/\pi$.

Each bend composing a single-lobe meander, or a compound bend meander, was identified by considering two consecutive inflexion points. Each bend was then resampled to contain the same number of points (i.e., 201), rotated to align its extremes with the x-axis, and saved on a specific dataset. This dataset, containing approximately 10 million of synthetically-generated bends, was subsequently divided into two independent sub-datasets, used afterwards for the training (8.5 million bends) and the testing (1.5 million bends) of the automatic classification procedure. The frequency distributions of the wavenumber λ and the parameters θ_1, θ_{3r} and θ_{3i} used in the Kinoshita curve are shown in Figure S1 of the Supporting Information.

2.2 Wavelet energy spectrum

The wavelet transform allows the analysis of temporal or spatial signals with a flexible time-frequency (or space-frequency) window (mother wavelet) that adjusts automatically, narrowing for high-frequency oscillations and widening for low-frequency oscillations (Antoine et al., 2004; Addison, 2018; Tary et al., 2018). In the present study, we have applied this analysis to the spatial distribution of the bend curvature $c(s)$.

The mother wavelet can, in general, be written as (Foufoula-Georgiou & Kumar, 1994):

$$\psi_{b,a}(s) = \frac{1}{\sqrt{a}}\,\psi\Big(\frac{s-b}{a}\Big), \tag{6}$$

where a is a positive scale parameter, and b is a real space parameter. The scale parameter controls the frequency by which the wavelet samples the curvature distribution, leading to either a dilatation ($a > 1$) or a contraction ($a < 1$) of the mother wavelet. The space parameter determines the sampling position along s of the mother wavelet.

The continuous wavelet transform of the curvature distribution is defined as

$$\Psi_c(b,a) = \frac{1}{\sqrt{a}} \int_{-\infty}^{\infty} c(s)\,\overline{\psi}_{b,a}(s)\,ds, \tag{7}$$

where an overbar denotes complex conjugate.

In general, a wavelet $\psi(s)$ and, in particular, the mother function must satisfy various conditions. It must have compact support or sufficiently fast decay to obtain localisation in space and have a zero mean,

$$\int_{-\infty}^{\infty} \psi(s)\,ds = 0. \tag{8}$$

Moreover, it must satisfy the admissibility condition.

$$C_\psi = 2\int_0^{\infty} \frac{\big|\widehat{\psi}(k)\big|^2}{k}\,dk < \infty, \tag{9}$$

where k is the wavenumber (i.e., the spatial frequency), and $\widehat{\psi}(k)$ is the Fourier transform of ψ, defined as

$$\widehat{\psi}(k) = \int_{-\infty}^{\infty} \psi\,(s)\,e^{-i\,k\,s}\,ds. \tag{10}$$

Mother wavelets can be defined in either the real or complex domain. In the case of complex wavelets, an additional requirement is that $\widehat{\psi}(k)$ must be real and vanish for negative wavenumbers ($k \le 0$). This type of wavelet, referred to as progressive, enhances the ability to identify singularities in the signal.

The inverse wavelet transform, allowing the reconstruction of the original curvature distribution, is defined as

$$c(s) = \frac{2}{C_\psi}\int_0^{\infty}\Big[\int_{-\infty}^{\infty} \Psi_c(b,a)\,\psi_{b,a}(s)\,db\Big]\,\frac{da}{a^2}. \tag{11}$$

It is easily demonstrated that the continuous wavelet transform is an energy-preserving transformation ensuring that (Foufoula-Georgiou & Kumar, 1994)

$$E_c = \int_{-\infty}^{\infty} \big|c(s)\big|^2 = \frac{2}{C_\psi} \int_0^{\infty} \int_{-\infty}^{\infty} \big|\Psi_c(b,a)\big|^2 \, db \, \frac{da}{a^2}. \tag{12}$$

The quantity $\Big|\Psi_c(b,a)\Big|^2/(C_\psi \, a^2)$ on the right-hand side of (12) can be interpreted as an energy density function on the (a,b)-plane, representing the energy on the scale interval Δa and spatial interval Δb, centred around the scale a and the position b. The quantity E_c thus quantifies the total energy in the wavelet spectrum of $c(s)$.

In this study, the PyWavelets Python package (Lee et al., 2019) was used to compute the continuous wavelet transform and the Mexican Hat.

$$\psi(s) = \frac{2}{\sqrt{3}\,\pi^{1/4}}(1-s)e^{-s^2/2} \tag{13}$$

was employed as mother wavelet.

2.3 Autoencoder

The total energy E_c of the wavelet spectrum for the channel axis curvature of each bed was represented through a greyscale image, with values ranging from 0 (black) to 256 (white) and a resolution of 64x64 pixels (Figure 2b). This simplified representation allowed the use of a smaller autoencoder with faster training.

In particular, we used a convolutional neural network autoencoder, consisting of a connected encoder and decoder. The encoder compresses each image into a low-dimensional latent representation while retaining as much essential information as possible from the high-dimensional initial space (Kingma & Welling, 2022). The decoder handles each latent space representation and reconstructs an output image that closely resembles the original input one (Goodfellow et al., 2016). The adopted autoencoder requires no supervision while training (Tschannen et al., 2018), and allows an efficient clustering in the latent space (Chadebec & Allassonniere, 2022).

The overall autoencoding process can be represented as

$$E_c = \mathcal{F}\big[\mathcal{G}(E_c)\big], \tag{14}$$

where $\mathcal{G}$ is the encoding function, and $\mathcal{F}$ is the decoding function. The neuronal networks associated with these two functions are trained such that

$$\underset{\mathcal{F},\mathcal{G}}{\operatorname{argmin}} \frac{1}{N} \sum_{i=0}^{N} \Delta\big\{E_{ci}, \mathcal{F}\big[\mathcal{G}(E_{ci})\big]\big\}, \tag{15}$$

where, N is the number of images used for the training, Δ is a loss function, defined as the binary cross-entropy measuring the binary logarithmic loss between predicted and true values (Creswell et al., 2017), and $\underset{\mathcal{F},\mathcal{G}}{\operatorname{argmin}}$ denotes the set of values of $\mathcal{F}$ and $\mathcal{G}$ for which the summation attains its minimum value.

The overall architecture of the autoencoder is summarised using the Visual Keras package (Gavrikov, 2020), as shown in Figure 3. The encoder consisted of a series of convolutional two-dimensional neural layers. Batch normalisation and flattening layers were used to encode the available information in a latent two-dimensional space. The decoder employed a series of transposed two-dimensional convolutional neural layers, followed by a batch normalisation layer. A convolutional two-dimensional neural layer was finally used to obtain the reconstructed image of the energy spectrum.

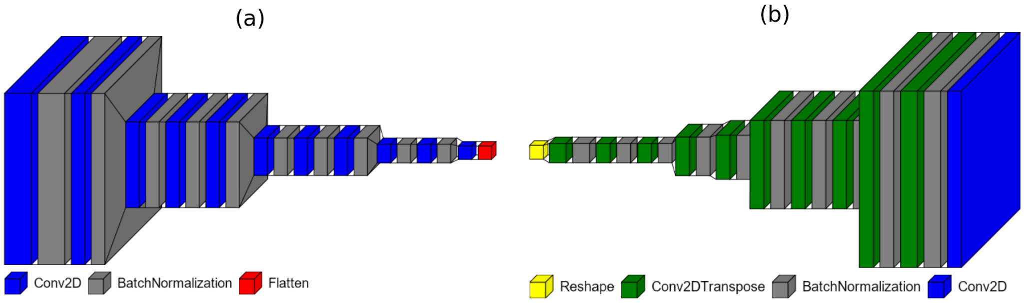

Figure 3. Autoencoder architecture. (a) Encoder and (b) Decoder.

The autoencoder was trained using the open-source TensorFlow software (Abadi et al., 2015). The bend curvature distributions computed from the Kinoshita-generated dataset were split into two independent subsets: 85% of bend curvature distributions were used for training, and the remaining 15% for validation. The error function selected for evaluating the correctness of the reconstructed images was a binary cross entropy function (Ruby et al., 2020), the binary loss being equal to 0 for a perfect model.

2.4 Clustering

The K-means algorithm (Brunton & Kutz, 2019) was used to find the optimal number of clusters characterising the image representation of E_c in the latent space. This optimal number was obtained by partitioning the data set into N_k groups S_i, such that the sum of squared deviations of the partitions is minimised. Denoting by $\mathcal{S}$ the generic partition, the function to be minimised is the within-cluster sum of squares $WCSS$, which can be formally expressed as (Kriegel et al., 2017)

$$WCSS = \sum_{S_i \in \mathcal{S}} \sum_{j=1}^{N_d} 2 \left|S_i\right| \sum_{\boldsymbol{x} \in S_j} (x_{ij} - \mu_{ij}). \tag{16}$$

Here, μ_{ij} is the mean coordinate of the cluster i in dimension j, $\left|S_i\right|$ is the cluster size, and the last summation defines the cluster variances. The minimisation of the function (16) was carried out through the Python package Scikit-Learn (Pedregosa et al., 2011).

2.5 Real meanders

The data-driven classification framework was first tested on an independent set of synthetically-generated bends, and then used to classify a set of 7521 real meander bends extracted from the datasets of Sylvester et al. (2019) and Lopez Dubon and Lanzoni (2019). The full list of the 32 meandering river reaches considered in the analysis is reported in Table S1 of the Supporting Information. Both datasets provide river planforms obtained by loading Google Earth maps in QGIS, zooming in on the river stretch of interest, drawing polylines along the river banks, and determining the centreline as the curve equidistant from each bank. This latter curve was smoothed out through a Savitzky-Golay filter (Savitzky & Golay, 1964) and a denoising wavelet filter (van der Walt et al., 2014) to reduce as much as possible spurious fluctuations when computing numerically the channel axis curvature.

The curvature was calculated by discretising the derivative $d\theta/ds$ in equation (3) through a second-order accurate central difference scheme for interior points, and either first or second-order accurate one-sided (forward or backward) differences at the boundaries, using the gradient function from the Python package numPy (Harris et al., 2020).

The along-river curvature distribution was then used to identify the inflexion points, where the curvature changed sign, and the bend apexes, where the curvature reached its maximum or minimum value. The position of inflexion points was finally used to recognise the sequence of single-lobe bends composing the river reach.

The noise in the numerically computed curvature can induce some small oscillations around zero and, consequently, the detection of spurious inflexion points. To avoid this problem only bends with a cartesian length L_x (Figure 1e) exceeding 5-8 the mean channel width, B_{mean}, were retained. Each single-lobe bend was eventually rotated to align the two inflexion points along the reference x-axis, and the platform was represented in the dimensionless cartesian plane $(x/B_{mean}, y/B_{mean})$.

Figure 4. (a) Localisation of the meandering rivers extracted from satellite images. The data refer to Lopez Dubon and Lanzoni (2019) except those with the superscript $*$ which refer to Sylvester et al. (2019). (b)-(j) Examples of parts of the meandering rivers extracted.

3 Results

Figure 5 shows an example of the automated classification procedure applied to a real river bend. In particular, Figure 5 (a) reports the planform of the bend plotted in the dimensionless cartesian plane, while the corresponding dimensionless curvature is plotted in Figure 5 (b) as a function of the curvilinear coordinate of the bend axis, scaled by its maximum length, s/s_{max}. The greyscale image of the total energy wavelet spectrum of the curvature distribution is reported in Figure 5 (c). Finally, Figure 5 (d) shows the correspondent image reconstructed through the trained autoencoder. The reconstructed image appears to capture the striking features of the original image. Overall the autoencoder performance in reconstructing the real meander data set resulted in a binary cross-entropy loss of just 0.1578. This close-matching reconstruction ensures a meaningful representation of the spectrum in the latent space, where compression of the information embedded in the spectrum facilitates cluster analysis.

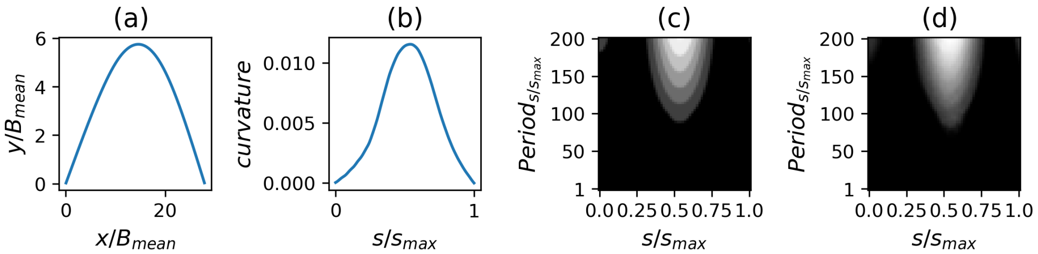

Figure 5. Example of application of the autoencoder to a real meander bend. (a) Bend shape plotted in the dimensionless plane (x/B_{mean},y/B_{mean}); (b) along-bend distribution of the channel axis curvature; (c) greyscale image of the total energy of the correspondent wavelet spectrum, with resolution 64×64 pixels and values ranging from 0 (black) to 256 (white); and (d) autoencoder reconstruction of the image.

As a preliminary step to the cluster analysis in the latent space, an additional criterion was applied to eliminate almost flat bends, typically associated with the very early evolution of a meander or multiple-lobe bends, which are not considered in the present analysis. Indeed, the energy spectrum of a nearly flat bend can be quite complicated, adding noise to the clustering procedure and making it less effective. Following Leopold and Wolman (1957), we assumed that bends belonging to a meandering reach have a sinuosity σ, defined as the ratio of intrinsic to cartesian length, larger than 1.5. The total number of meandering bends to be classified thus reduced from 7521 to 1911. The application of the K-means algorithm to this set of bends in the latent space yielded a number of clusters equal to 3. Increasing this number did not produce any significant improvement in minimising the within-cluster sum of squares defined by (16), as shown by Figure S2 in the Supporting Information.

Figure 6 summarises the results of the cluster analysis in the two-dimensional latent space, where three distinct clusters are discernible (Figure 6a). The bend shapes in the dimensionless plane $x/B_{mean}, y/B_{mean}$ corresponding to the three centroids are plotted in Figure 6b,c,d. They represent the characteristic bend shape typical of each cluster. Cluster C1 is characterised by symmetrical bends (Figure 6b), whereas clusters C2 and C3 are composed of downstream-skewed (Figure 6c) and upstream-skewed (Figure 6d) bends, respectively. The majority of data falls into cluster C1 (44% bends), followed by cluster C2 (36% bends) and cluster C3 (20% bends). On the other hand, the data dispersion within each cluster, defined as the ratio of standard deviation of the distance from the cluster centroid to the mean, is greater for cluster C3 (3.271), followed by cluster C2 (2.356), and cluster C1 (2.292).

The percentages of each bend type contained in the 32 river reaches considered in the present study are shown in Figure 7. Symmetrical bends (C1) prevail in 22 of the 32 river

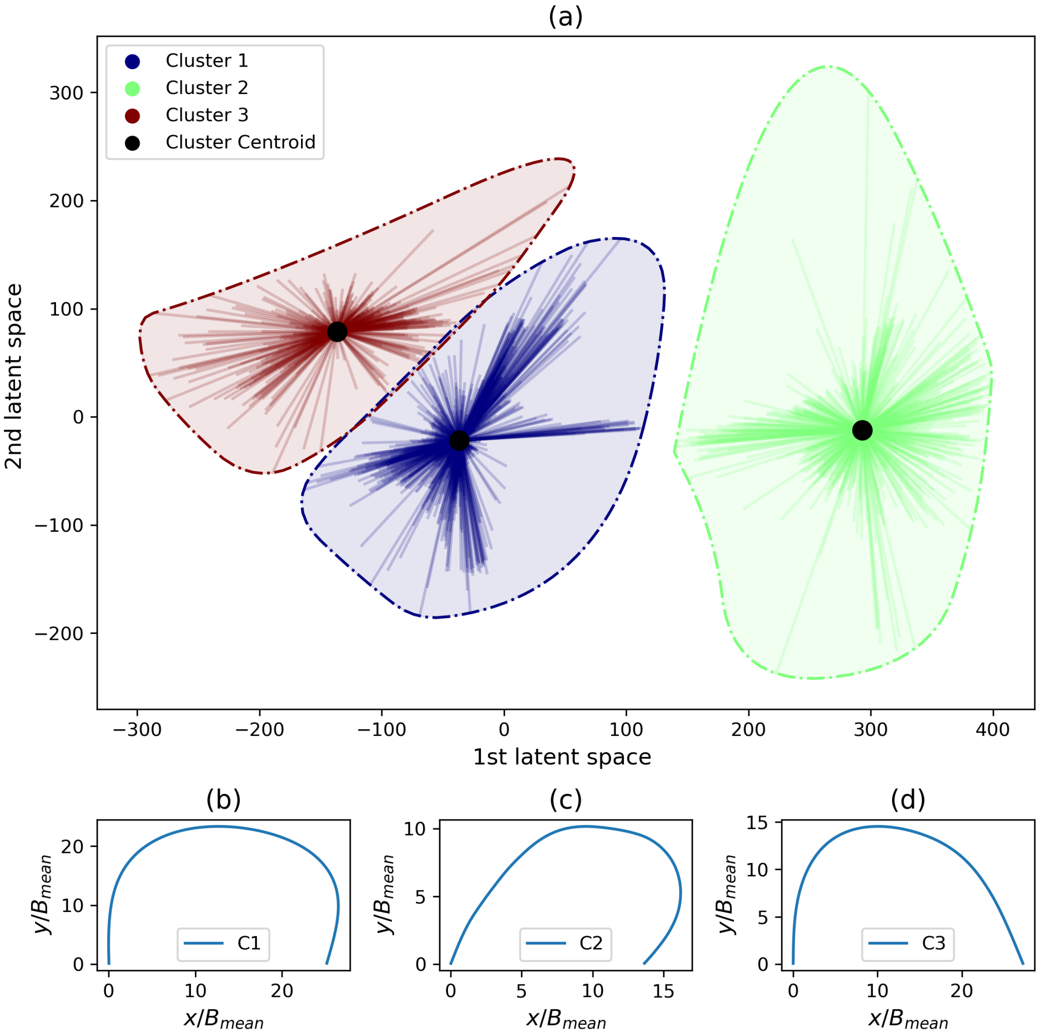

Figure 6. (a) Results of the cluster analysis in the two-dimensional latent space. Bend shapes corresponding to the centroid of (b) cluster C1, (c) cluster C2, and (d) cluster C3. The solid lines within each cluster connects each point to its centroid giving a visual representation of the cluster dispersion. The dashed-line connects the points located farther away from the centroid showing the cluster boundary.

reaches, whereas 10 out of 32 rivers exhibit a predominance of downstream-skewed bends. None of the investigated rivers had a predominance of upstream-skewed bends.

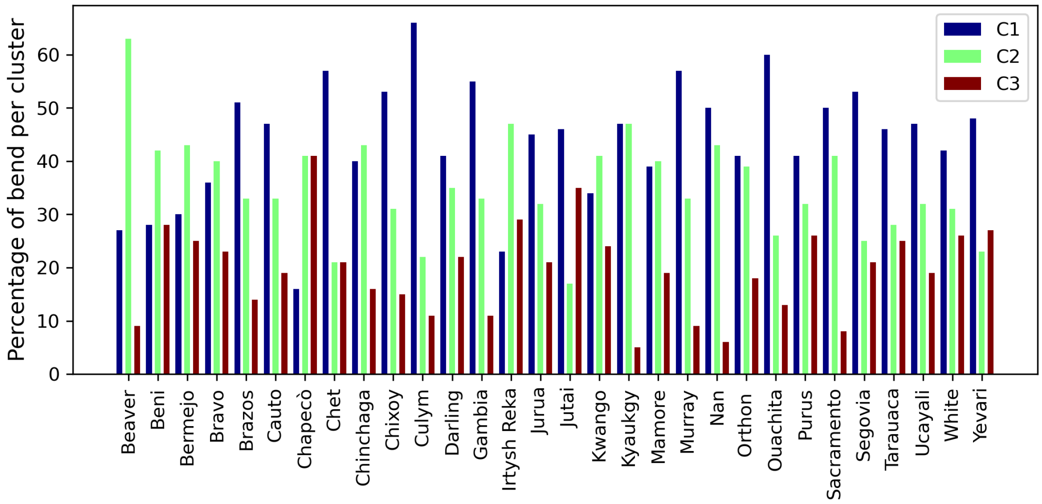

Figure 7. Percentages of the three bend types (C1, symmetrical; C2, downstream skewed; and C3, upstream skewed) emerging from the clustering analysis are reported for each of the meandering rivers reaches, as localised in Figure 4.

4 Discussion

The use of the Kinoshita curve (equation 2) was fundamental to produce a sufficient amount of data for training the autoencoder. This is particularly relevant, considering the vast effort required to extract river planforms from satellite images, as well as the river width needed for normalisation and comparison (Finotello et al., 2018). Moreover, the values of the loss function used to evaluate the autoencoder (0.1313 and 0.1312 for the training and evaluation set, respectively) indicate that, when applied to real rivers, the information lost in the latent space is reasonably small. This result confirms the reliable reconstruction of most of the energy spectrum images and, hence, a successful transfer of knowledge from the synthetic data used for training to real data.

Even though real bends with a sinuosity smaller than 1.5 were excluded from the classification analysis, some peculiar bend shapes remained included in the dataset. A few examples are shown in Figure 8a. Essentially, they are bends with small amplitude A as compared to their cartesian wavelength L_x, and relatively high sinuosity. To identify these particular bends, we introduces an Index of Maturity (I_M) defined as

$$I_M = \frac{A}{L_x}. \tag{17}$$

The values of the sinuosity and the Maturity Index for each meander bend are shown in Figure 8 (b), including all the bends extracted from the various river reaches, independently of the sinuosity. The point cloud seemingly has a lower-limit boundary that depends on the Maturity Index. This boundary has a shape that can be reasonably approximated though the parabola

$$\sigma = 2\, I_M \sqrt{1 + \frac{1}{4 I_M^2}}. \tag{18}$$

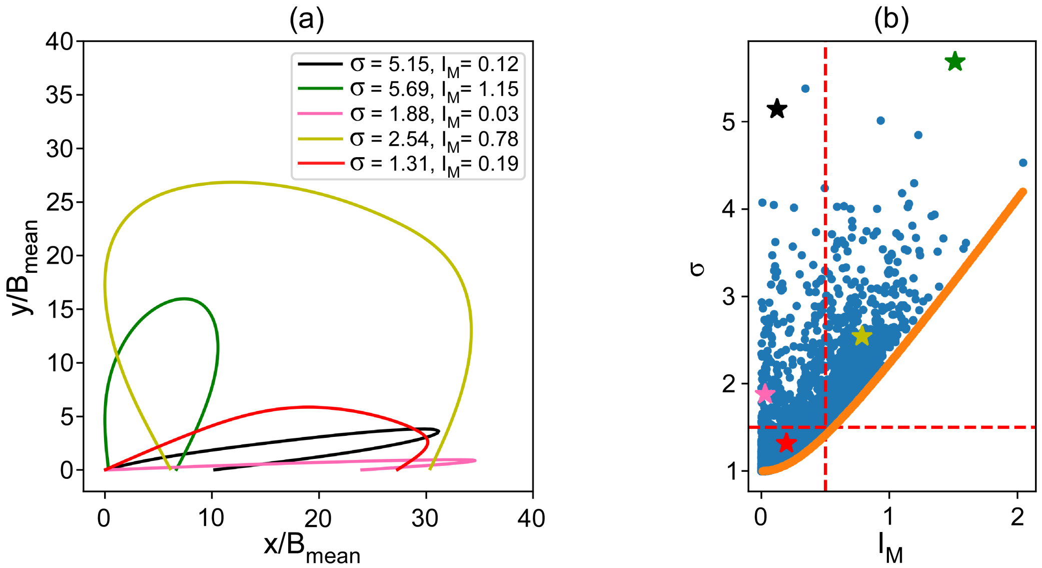

Figure 8. (a) Examples of the dependence of bend shapes from the values of σ and I_M. (b) The bend sinuosity σ is plotted as a function of the maturity index I_M for all the bends extracted from the investigated river reaches.

Figure 8 suggests that both the sinuosity and the Maturity Index can be used to identify bends with relatively uncommon shapes. Bends with $\sigma < 1.5$ are assumed to belong to nearly straight reaches, according to the classification proposed by Leopold and Wolman (1957). The line $\sigma = 1.5$ intercepts the lower-limit boundary for $I_M \simeq 0.56$. This latter value can be used to discriminate bends with small amplitude as compared to the wavelength ($I_M \lesssim 0.5$), leading to the peculiar shapes shown in Figure 8(a). This type of bends represents 25.4% of the total bends analysed. Excluding these bends from the cluster analysis does not change significantly the classification outputs. The number of clusters remains still equal to 3, with shapes representative of the corresponding centroids remarkably similar to those shown in Figure 6(b)-(d) (see Figure S3 in the Supporting Information). The criterion based on a lower threshold for I_M essentially identifies uncommon, nearly flat shapes, which have a limited overall impact on the automated classification procedure.

The sinuosity has a major role in identifying the degree of evolution of a given bend. Low-sinuosity bends usually represent the early stages of evolution, whereas high values of sinuosity are likely associated with bends in a more advanced stage of evolution. The statistical analysis carried out by Bolla Pittaluga and Seminara (2011) revealed that the meander bends in the database of Lagasse et al. (2004) have a median sinuosity of 1.7 and a standard deviation of 0.4. Bends with high sinuosity ($\sigma \gtrsim 3 - 3.5$) are likely to be relatively infrequent. This fact is confirmed by Figure 9, showing the box plot characterisation of the sinuosity distribution within each of the three clusters identified by the automated classification procedure. The values of the median sinuosity σ_m agree with those estimated for the database of Lagasse et al. (2004), with some slight variations from one cluster to another. In particular, the higher median value is observed for downstream-skewed bends (cluster C2, $\sigma_m = 2.014$), the smallest median value characterises upstream-skewed bends (cluster C3, $\sigma_m = 1.720$), while symmetrical bends (cluster C1) have $\sigma_m = 1.906$. The data dispersion, measured through the distance between the upper and lower quartiles (Interquartile Range, IQR), is highest for the downstream-skewed bends ($IQR = 0.758$), whereas upstream-skewed bends have the lowest degree of variation ($IQR = 0.305$). The trend of the sinuosity distribution for symmetrical bends is intermediate between the other two classes. Each cluster shows several upper outliers, i.e, larger than 1.5 times the interquartile range. In contrast, lower outliers are invariably absent. This absence is due to the choice of excluding bends with sinuosity lower than 1.5. The smallest number of outliers (6/435, $\sim$ 1.5%) is observed for upstream-skewed bends (C2, whereas the largest number (41/858, $\sim$ 5%) characterises the symmetrical bends (C1), which can be considered as a transition pattern between upstream-skewed (C3) and downstream-skewed (C2) bends (or vice versa).

The above results may be partly explained in light of existing theoretical studies of river meandering. According to the nonlinear bend instability analysis performed by Seminara et al. (2001), and confirmed by the results of numerical simulations up to incipient cutoff conditions (Lanzoni & Seminara, 2006), symmetrical bends mainly form during the initial evolution stages of a train of meanders developing along an initially straight, slightly-perturbed channel. In this phase, it is the first harmonic of the curvature, i.e. associated with the term $\cos(\lambda\, s)$ of equation (3), which grows almost linearly in time. The occurrence of skewed bends arises at a later stage of evolution due to slower nonlinear growth of the third harmonic $\cos(3\,\lambda\, s)$. During the first linear phase, the meander length increases slowly, while meander elongation is faster during the second phase, leading to the formation of fattened and skewed meander shapes. Bend amplification is initially quite slow, increases reaching a maximum, and then decreases slowly up to incipient cutoff conditions, as also observed in the field by Nanson and Hickin (1983). Conversely, the rate of lateral bend migration, which is quite fast at the beginning of the evolution, tends to progressively slow down up to almost vanishing before a neck cutoff. The direction of bend skewing is dictated by the morphodynamic regime characterising the river reach. This regime depends on the value of the width-to-depth ratio β with respect to its resonant value β_R. This latter value, in turn, is controlled by the Shields stress, τ_*, and the sediment grain size scaled with the uniform flow depth, d_s (Seminara & Tubino, 1992). For values of $\beta < \beta_R$ (sub-resonant regime), bends are upstream skewed and migrate downstream. Conversely, in the super-resonant regime ($\beta > \beta_R$), bends are downstream skewed and migrate upstream. As a meandering reach evolves, changes in the average reach slope, either due to the elongation of meander bends as they progressively grow or the shortening of the river path resulting from cutoffs, lead to variations of the reach-averaged values of β, and well as τ_* and d_s and, consequently, β_R. This can induce a change of the morphodynamic regime for values of β close to β_R, promoting the development of symmetrical bends (Zolezzi et al., 2009).

Within this general theoretical framework, higher variations in the sinuosity likely indicate the presence of a larger number of bends at different stages of evolution and, consequently, a potentially more dynamic river reach. Symmetrical bends can be associated to either relatively young evolution stages (e.g., those characterising a recently straighten, weakly sinuous reach) or to more advanced, higher sinuosity stages, as those linked to the change in morphodynamic regime when the evolving river reach approaches resonant conditions. Symmetrical bends may also be part of meanders with multiple loops (i.e., including multiple inflexion points), not accounted for in the present automated classification framework, which assumes a meander always delimited by two consecutive inflexion points of the channel axis curvature. The various origins of symmetrical bends may explain the greater number of outliers exhibited by the C1 cluster. Skewed bends, on the other hand, should, in general, represent more advanced stages of meander evolution, associated with higher values of sinuosity. This is indeed verified in Figure 9 for downstream-skewed bends but not for upstream-skewed bends, which have a median sinuosity also smaller than that of symmetrical bends. On the other hand, the number of upstream-skewed bends (distinctive of sub-resonant conditions) is noticeably lower than that of both downstream-skewed bends (typical of super-resonant conditions) and symmetrical bends. This lower number potentially explains the lower variability of the sinuosity and the smaller number of outliers characterising upstream-skewed bends. Notably, the prevalence of super-resonant bends over sub-resonant ones agrees with the mechanistic analysis carried out by Zolezzi et al. (2009) on a dataset comprising more than 100 gravel-bed rivers.

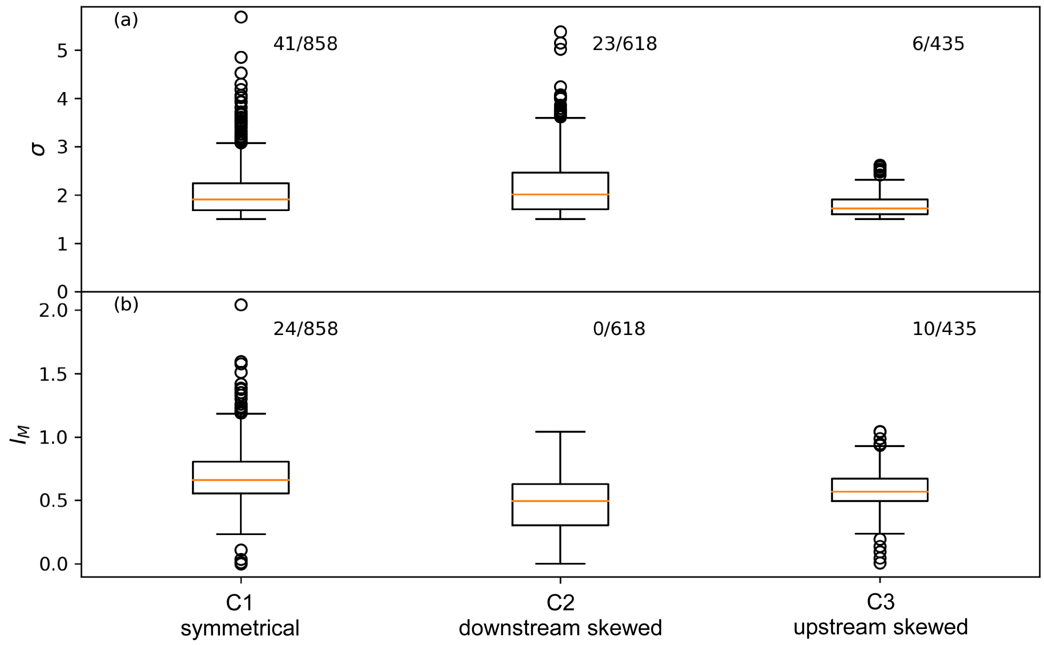

Figure 9. Box plot representation of (a) the sinuosity and (b) the Maturity Index values within each of the three clusters recognised by the automated classification procedure. The red lines indicate the median values, while the lower and upper sides of the boxes correspond to the first and third quartiles, respectively. The lower and higher horizontal segments denote the whiskers, defined as 1.5 times the interquartile range (IQR). The numbers in the upper part of the plot, indicate the the number of outliers, which are marked by empty circles, and the size of the sample.

Additional sources of complexity in interpreting the results of the automated classification are due to cutoff events, the heterogeneous composition of the floodplain, and the mutual morphodynamic influence between adjacent bends at different stages of evolution. Repeated cutoffs generally contribute to limiting the mean bend sinuosity within a given river reach, determining a continuous sequence of sinuosity fluctuations around the mean value, as shown by long-term numerical simulations (Frascati & Lanzoni, 2010). The heterogeneous composition of the floodplain may influence the intensity of these sinuosity variations (see, e.g., Figure 5c,f in Bogoni et al., 2017). The growth of a given meander bend is influenced by the evolution of the adjacent bends. In general, morphodynamic information associated with the evolution of planform waves and river bed topography propagates mainly downstream in the sub-resonant regime, while is primarily felt upstream in the super-resonant regime (Zolezzi & Seminara, 2001; Lanzoni & Seminara, 2006). The type of morphodynamic regime, in turn, depends on the hydraulic and sedimentological parameters characterising the river, as well as the mechanism dominating sediment transport (e.g. bedload in gravel-bed rivers and suspended load in sandy rivers). Finally, temporal variations in the hydrological forcing and spatial heterogeneity in the sediment composition add a further degree of difficulty in the interpretation of the statistical distribution of σ and I_M for the three classified shapes.

The potential of the automated classification procedure was tested on a highly active reach of the Ucayali River, which registered several cutoffs in the period 1984-2015 (Schwenk et al., 2017; Lopez Dubon & Lanzoni, 2019). The investigated reach is located in the Peruvian Amazon basin and has a cartesian length of about 54 km, extending approximately from Atalaya (10.7318° S, 73.7586°° W) to Pucallpa (8.3929° S, 74.5826°° W), with an average slope in the range 1-10$\times 10^{-5}$ (Santini et al., 2015). The mean annual discharge and the average maximum discharge at Pucallpa are 9720 m^3/s and 16370 m^3/s, respectively (Alvarado-Ancieta & Ettmer, 2008; Santini et al., 2015). The bed sediment has a mean size ranging from 0.17 to 0.39 mm (ECSA, 2005), with a $d_{50} \simeq 0.3$ mm at Pucallpa (Ettmer & Alvarado-Ancieta, 2010). The reach averaged channel width, estimated from satellite images, varied in the range 668-954 m (mean value 742 m) depending on the planform configuration of the river over the years. Similarly, the reach sinuosity varied between 2 and 2.6, with a mean value of 2.3. The water depth ranges between 7 m and 15 m. These variations are associated with the progressive elongation of the intrinsic river length due to meander growth and the abrupt shortening consequent to cutoffs (Figure 10a-e), and lead to continuous fluctuations in the reach average slope.

Figure 10f shows the results of the automated classification procedure throughout the considered 32 years. The investigated river reach presents predominantly symmetric bends (cluster C1) for a total of 25 years, downstream-skewed bends (cluster C2) for a total of 6 years, and a single year (1990) with prevailing upstream-skewed bend (cluster C3). The temporal distribution of the percentage of skewed bends could be interpreted as the result of the occurrence of various transitions from one morphodynamic regime to another triggered by significant cutoff events. To test this hypothesis, we computed the yearly value of the resonant value of the half-width to depth ratio β_R using the fully coupled, linearised morphodynamic model of Zolezzi and Seminara (2001). The initial (1984) planform configuration was characterised by a sinuosity of 2.12 and an average channel width of 786 m. Assuming uniform flow conditions and a plane bed (confirmed *a posteriori* by the bed classification procedure of Simons and Richardson (1966)), the average maximum discharge (16370 m^3/s) is conveyed through an equivalent rectangular cross-section with a depth of 10 m for a slope 5×10^{-5}. These conditions correspond to a half-width to depth ratio β of 39.3, a Shields stress τ_* of 1, and a dimensionless grain size d_s of 3×10^{-5}, consistent with values typically observed in sandy rivers (Francalanci et al., 2020). The resonant value of the half-width to depth ratio corresponding to this set of dimensionless parameters is $\beta_R = 29.54$. As the reach sinuosity evolves over time, the parameter values also vary accordingly. It can be easily demonstrated that (Zolezzi et al., 2009):

$$\frac{\beta}{\beta_0} = \Big[\sigma \, \frac{C_f}{C_{f0}} \Big(\frac{B_0}{B}\Big)^3\Big]^{1/3}, \qquad \frac{d_s}{d_{s0}} = \Big[\frac{1}{\sigma} \, \frac{C_{f0}}{C_f} \Big(\frac{B}{B_0}\Big)^2\Big]^{1/3}, \qquad \frac{\tau_*}{\tau_{*0}} = \frac{1}{\sigma^{2/3}} \Big(\frac{C_f}{C_{f0}} \Big(\frac{B_0}{B}\Big)^2\Big)^{1/3}. \tag{19}$$

where C_f is the friction coefficient ($C_f = [6 - 2.5 \ln(2.5\, d_s)]^{-2}$ for plane bed conditions), and a sub-script 0 denotes the initial year.

The time series of β and β_R resulting from the analysis are shown in Figure 10h. It appears that the transition from a super-resonant dominated behaviour (epitomised by a prevalence of upstream-skewed C3 bends) to a sub-resonant dominated behaviour (embodied by a dominance of downstream-skewed C2 bends), and vice versa, is indeed plausible and is favoured by the abrupt decrease of sinuosity after big cutoffs. This is, for instance, the case of the 1992-1993 and 2004-2005 cutoffs, which likely led to a transition from a sub-resonant to a super-resonant regime. Remarkably, each passage through resonant conditions seems to enhance the formation of symmetrical C1 bends. Overall, the temporal distributions of morphodynamic regimes resulting from comparing the magnitude of β with respect to β_R and that inferred from the percentage of C2 and C3 bends is reasonable, though not perfect. This can be due to many aspects, such as the uncertainties on the hydraulic parameters adopted for the computations of β and β_R, as well as the simplifications embedded in the morphodynamic model, which consider an equivalent rectangular cross-section and does not account explicitly for suspended load effects. Moreover, deducing the dominant morphodynamic regime only from the percentages of bend classes present in the entire river

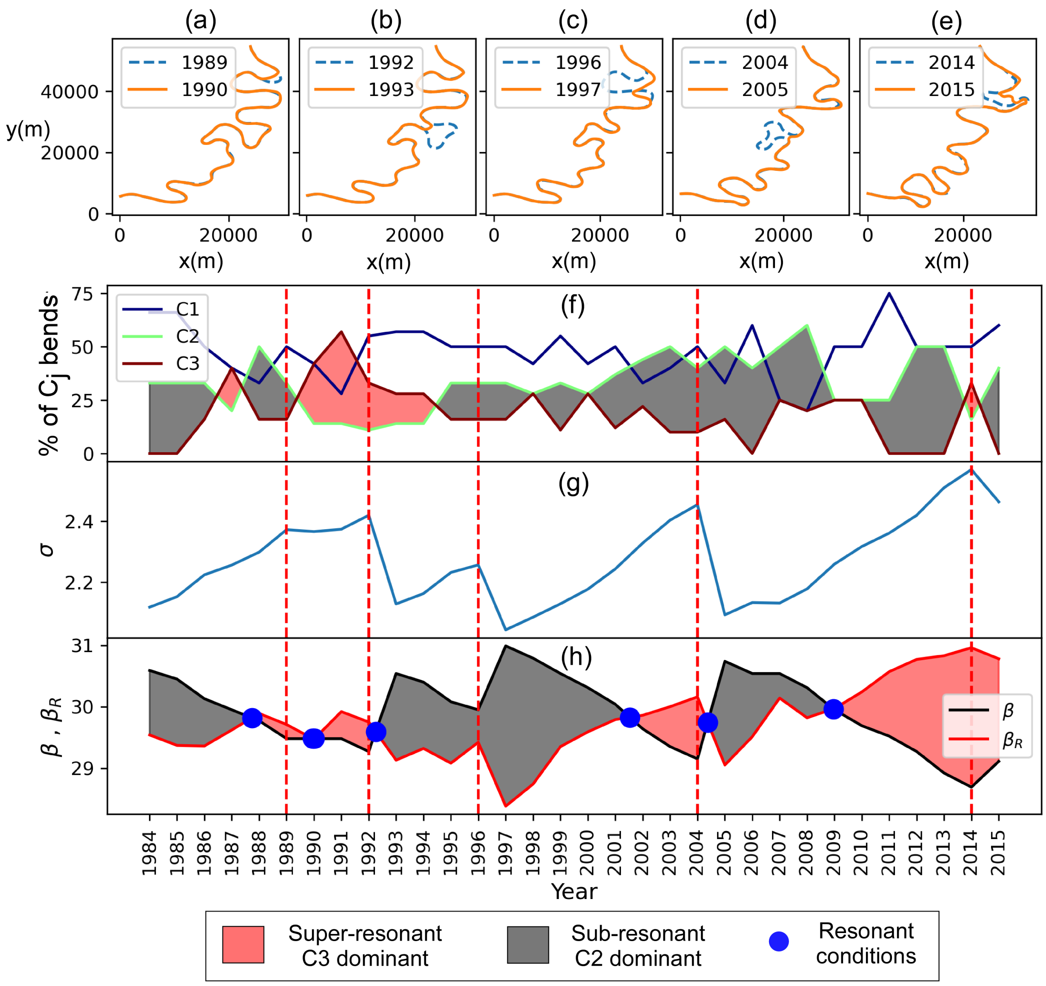

Figure 10. (a)-(e) Planforms before and after major cutoff events occurring from 1984 to 2015 along the reach of the Ucayali River comprised between Atalaya and Pucallpa. (f) The percentage of meander classes detected along the reach over various years. Temporal evolution of (f) the sinuosity distribution and (h) the values of the half-width to depth ratio, β, and the corresponding resonant value, β_R. The latter has been computed for plane bed conditions, using the total load transport formula of Engelund and Hansen (1967), and setting equal to 0.55 the coefficient accounting for gravitational effect on the transverse direction of bedload (Frascati & Lanzoni, 2013). Red dashed lines represent the cutoff events.

reach does not account for the possible inclusion of a bend in composite or multi-lobed patterns. The application of the classification procedure described above should then be regarded as a significant example of how it, in conjunction with theoretical arguments, can help to unravel the morphodynamic behaviour of a given river reach.

4.1 Limitations of the study and future work

This study proposes a data-driven classification method for single-lobe meanders, informed by the images of total energy in the wavelet spectrum of the bend curvature. This automated approach provides valuable insight for the detection and classification of single bends along a meandering river. Rather than directly analysing bend planforms, it objectively analyses the energy spectrum inherent in bend shapes without requiring the introduction of any geometric metrics, unlike previous classification approaches based on bend shape matching. The complexity of meander shapes is accounted for through the large number of parameters comprising the autoencoder architecture. The physics-based nature of the classification stems from the control exerted by bed axis curvature on migration rates, sediment transport and sorting (e.g., Güneralp & Rhoads, 2008; Finotello et al., 2018; Donovan et al., 2021). Nevertheless, some limitations of the study are worth mentioning.

The autoencoder-based classification model was trained on single-lobe bends, delimited by two consecutive inflexion points of the channel axis curvature. These bends were extracted from planforms generated synthetically using the Kinoshita curve. However, these planforms also include multiple-lobe meanders composed of various single-lobe bends. The automated procedure does not recognise these multiple-lobe shapes, and an additional, non-trivial effort is needed to include them in the classification.

The training dataset was extensive, containing $\sim 10^7$ Kinoshita-generated meanders. Despite the complex and varied shapes exhibited by real meanders, the size of this dataset could be reduced without losing the classification effectiveness. Other machine-learning classifiers need to be tested to capture the essential features of articulated meander shape features by using a smaller training dataset. This could also be particularly useful for classifying multi-lobed meanders.

The classification was based on greyscale images representing the total energy wavelet spectrum of the spatial distribution of bend curvature. For each image, the total energy was scaled according to the maximum value characterising the considered bend. This bend-specific scaling is independent of the total energy of the other bends in the dataset. The use of greyscale images simplifies the representation by limiting possible numerical values for the autoencoder, and the single scale per image preserves more features compared to normalization based on the complete dataset.

The boundaries of each cluster in Figure 6 were determined by smoothly connecting the points farthest from the centroid. Consequently, they may be sensitive to the inclusion of new data points, making it difficult to classify any point in their proximity with a high degree of confidence. This is particularly significant for clusters quite close in the latent space, as C1 and C3.

Finally, the present study is focused on single-lobe meanders, with multi-lobe meanders split into simple bends. Thus, The wavelet analysis gives information on each bend, without considering how the bends are linked. Single bends composing a multi-lobe meander are not necessarily all skewed in the same direction of the compound shape. Hence, inferring the morphodynamic regime from the prevailing percentage of single skewed (either upstream or downstream) bends must be taken with some caution. In other words, splitting composed meanders into their single bend components, as commonly done in practice, implies a loss of information in determining the morphodynamic regime based on the prevailing bend skewness.

5 Conclusions

This study developed a data-driven classification framework for meander bends based on the total energy of the wavelet spectrum of bend curvature distribution. Kinoshita-generated bends were generated, creating a large dataset. An autoencoder based on a convolutional neural network was trained and validated using this dataset. The trained neural network was then tested on remotely sensed meanders. The main findings resulting from the application of the trained neural network model are summarised below.

Investigating the energy spectrum of bend curvature through a continuous wavelet transform ensures a solid physical foundation. Curvature controls the flow field and the bed topography, ultimately correlating with meander migration, sediment transport, and grain sorting.

The autoencoder successfully transferred knowledge from Kinoshita-generated bends to real data, resulting in low binary cross-entropy loss (0.1578) for real meander. This value is quite close to the loss (0.1333) achieved for the independent Kinoshita-generated dataset used for validation.

The unsupervised classification model identified three main categories of meandering river bends: symmetric, downstream-skewed, and upstream-skewed. Applying this method to the real meander data set extracted from satellite images revealed that the symmetric single-bend meander shape is the most predominant.

An application of the classification method to a reach of the Ucayali River highlighted how the planform dynamics over a span of 32 years, from 1984 to 2015, may produce a shift in the dominant bend class. The shortening of the reach due to the cutoffs may, in fact, lead to a transition from super-critical to sub-critical conditions (or vice versa), resulting in a shift from dominant downstream-skewed bends to upstream-skewed bends (or vice versa).

In summary, this study introduced a novel framework for classifying single-lobe meander bends based on the total energy in the wavelet energy spectrum of bend curvature. This classification tool aids in identifying patterns in meander evolution, thereby potentially enhancing the effectiveness of river management interventions. A logical next step for improvement lies in extending the methodology to handle compound and multiple-lobe meanders.

Data Availability Statement

Remotely-sensed meanders were taken from datasets reported in Sylvester et al. (2019) (`https://github.com/zsylvester/curvaturepy`) and Lopez Dubon and Lanzoni (2019) (`https://zenodo.org/record/1467638\#.W83q-UvHxPY`). The link to the repository for the trained classification model is about to be created.

Author contributions

The authors contributed equally to the paper.

Competing interests

The authors declare that they have no conflict of interest.

Acknowledgments

S.L.D. acknowledges the support from the European Union Horizon 2020 research and innovation programme under the Marie Sklodowska-Curie grant agreement No. 801215 and the University of Edinburgh Data-Driven Innovation programme, part of the Edinburgh and South East Scotland City Region Deal. S.L. acknowledges the use of the AI tool "ChatGPT" (`chat.openai.com`) to check the English.

References

Abadi, M., Agarwal, A., Barham, P., Brevdo, E., Chen, Z., Citro, C., ... Zheng, X. (2015). *TensorFlow: Large-scale machine learning on heterogeneous systems.* Retrieved from `https://www.tensorflow.org/` (Software available from tensorflow.org)

Addison, P. S. (2018). Introduction to redundancy rules: the continuous wavelet transform comes of age. *Philosophical Transaction of the Royal Society A*, *376*(20170258), 1–15. doi: 10.1098/rsta.2017.0258

Alvarado-Ancieta, C., & Ettmer, B. (2008). Morfología fluvial y erosión en curvas abruptas del Río Ucayali, Perú. *Revista de Interdisciplinaria de Cienca y Tecnología del Agua, Ingeniería Hidráulica en méxico*, *XXIII*(6), 69–90. (ISSN-0186-4076)

Antoine, J.-P., Murenzi, R., Vandergheynst, P., & Ali, S. T. (2004). Warm-up: the 1-D continuous wavelet transform. In *Two-dimensional wavelets and their relatives* (p. 1-31). Cambridge University Press. doi: 10.1017/CBO9780511543395.002

Bellizia, E., Tognin, D., Boaga, J., Cassiani, G., Leardi, R., Finotello, A., ... Ghinassi, M. (2022). From electromagnetic to sediment textural maps: an integrated approach to unravel the intra-point-bar variability of sediment properties. *Journal of the Geological Society*, *179*(4), 1–12. doi: 10.1144/jgs2021-156

Blondeaux, P., & Seminara, G. (1985). A unified bar-bend theory of river meanders. *Journal of Fluid Mechanics*, *157*, 449–470. doi: 10.1017/S0022112085002440

Bogoni, M., Putti, M., & Lanzoni, S. (2017). Modeling meander morphodynamics over self-formed heterogeneous floodplains. *Water Resources Research*, *53*(6), 5137–5157. doi: 10.1002/2017WR0207266

Bolla Pittaluga, M., & Seminara, G. (2011). Nonlinearity and unsteadiness in river meandering: A review of progress in theory and modelling. *Water Resources Research*, *38*(20), 20–38. doi: 10.1002/esp.2089

Bozzolan, E., Brenna, A., Surian, N., Carbonneau, P., & Bizzi, S. (2023). Quantifying the Impact of Spatiotemporal Resolution on the Interpretation of Fluvial Geomorphic Feature Dynamics From Sentinel 2 Imagery: An Application on a Braided River Reach in Northern Italy. *Water Resources Research*, *59*(12), 1–15. doi: 10.1029/2023WR034699

Brice, C. J. (1973). Meandering Pattern of the White River in Indiana: an Analysis. In M. Morisawa (Ed.), *Fluvial Geomorphology* (pp. 178–200). State University of New York.

Brice, C. J. (1974). Evolution of meander loops. *Geological Society of America Bulletin*, *85*(4), 581–586. doi: 10.1130/0016-7606(1974)85⟨581:EOML⟩2.0.CO;2

Brunton, S. L., & Kutz, J. N. (2019). Machine learning and data analysis. In *Data-Driven Science and Engineering: Machine Learning, Dynamical Systems, and Control* (pp. 115–116). Cambridge University Press. doi: 10.1017/9781108380690

Buffington, J. M., & Montgomery, D. R. (2013). Geomorphic classification of rivers. In J. Shroder & E. Wohl (Eds.), *Treatise on Geomorphologyy* (Vol. 9, pp. 730–767). Academic Press, San Diego, CA. doi: 10.1016/B978-0-12-374739-6.00263-3

Camporeale, C., Perona, P., Porporato, A., & Ridolfi, L. (2005). On the long-term behavior of meandering rivers. *Water Resources Research*, *41*(12), 1–13. doi: 10.1029/2005WR004109

Camporeale, C., Perona, P., Porporato, A., & Ridolfi, L. (2008). Significance of cutoff in meandering rivers dynamics. *Journal of Geophysical Research*, *113*(F1), 1–11. doi: 10.1029/2006JF000694

Camporeale, C., Perucca, E., Ridolfi, L., & Gurnell, A. M. (2013). Modeling the interactions between river morphodynamics and riparian vegetaion. *Reviews of Geophysics*, *51*(3), 379–414. doi: 10.1002/rog.20014

Chadebec, C., & Allassonniere, S. (2022). A geometric perspective on variational autoencoders. In S. Koyejo, S. Mohamed, A. Agarwal, D. Belgrave, K. Cho, & A. Oh (Eds.), *Advances in neural information processing systems* (Vol. 35, pp. 19618–19630). Curran Associates, Inc. Retrieved from `https://proceedings.neurips.cc/paper_files/paper/2022/file/7bf1dc45f850b8ae1b5a1dd4f475f8b6-Paper-Conference.pdf`

Creswell, A., Arulkumaran, K., & Bharath, A. A. (2017). *On denoising autoencoders trained to minimise binary cross-entropy.*

Crosato, A. (1990). *Simulation of meandering river processes* (Communication on Hydraulic and Geotechnical Engineering, Report 90-3). Delft (NL): Delft University of Technology.

Donovan, M., Belmont, P., & Sylvester, Z. (2021). Evaluating the relationship between meander-bend curvature, sediment supply, and migration rates. *Journal of Geophysical Research: Earth Surface*, *126*(3), 1–20. doi: 10.1029/2020JF006058

ECSA, H. (2005). *Estudio de la navegabilidad del Río ucayali en el tramo comprendido entre pucallpa y la confluencia con el Río Marañon.* Dirección general de transporte acuático, Ministerio de Transportes y Comunicaciones, Lima, (PE).

Engelund, F., & Hansen, E. (1967). *A monograph on sediment transport in alluvial streams.*

Ettmer, B., & Alvarado-Ancieta, C. A. (2010). Morphological development of the Ucayali River, Peru without human impacts. *Waldökologie, Landschaftsforschung und Naturschutz*, *10*, 77–84.

Finotello, A., D'Alpaos, M., A. Bogoni, Ghinassi, M., & Lanzoni, S. (2020). Remotely-sensed planform morphologies reveal fluvial and tidal nature of meandering channels. *Scientific reports*, *10*(54), 1–13. doi: 10.1038/s41598-019-56992-w

Finotello, A., Lanzoni, S., Ghinassi, M., Marani, M., Rinaldo, A., & D'Alpaos, A. (2018). Field migration rates of tidal meanders recapitulate fluvial morphodynamics. *Proceedings of the National Academy of Sciences*, *115*(7), 1463–1468. doi: 10.1073/pnas.171133011

Foufoula-Georgiou, E., & Kumar, P. (Eds.). (1994). *Wavelets in geophysics* (Vol. 4). AcademicPress.

Francalanci, S., Lanzoni, S., Solari, L., & Papanicolaou, A. N. (2020). Equilibrium cross section of river channels with cohesive erodible banks. *Journal of Geophysical Research: Earth Surface*, *125*, 1-20. doi: 10.1029/2019JF005286

Frascati, A., & Lanzoni, S. (2009). Morphodynamic regime and long-term evolution of meandering rivers. *Journal of Geophysical Research*, *114*(F2), 1–12. doi: 10.1029/2008JF001101

Frascati, A., & Lanzoni, S. (2010). Long-term river meandering as a part of chaotic dynamics? A contribution from mathematical modelling. *Earth Surface Processes and Landforms*, *35*(7), 791–802. doi: 10.1002/esp.1974

Frascati, A., & Lanzoni, S. (2013). A mathematical model for meandering rivers with varying width. *Journal of Geophysical Research: Earth Surface*, *118*(3), 1641–1657. doi: 10.1002/jgrf.20084

Gavrikov, P. (2020). *visualkeras.* `https://github.com/paulgavrikov/visualkeras`. GitHub.

Goodfellow, I., Bengio, Y., & Courville, A. (2016). *Deep learning.* MIT Press. Retrieved from `http://www.deeplearningbook.org`

Güneralp, I., Abad, J. D., Zolezzi, G., & Hooke, J. M. (2012). Advances and challenges in meandering channels research. *Geomorphology*, *163-164*, 1–9. doi: 10.1016/j.geomorph.2012.04.011

Güneralp, I., & Rhoads, B. L. (2008). Continuous characterization of the planform geometry and curvature of meandering rivers: Planform geometry and curvature of meandering rivers. *Geographical Analysis*, *40*, 1–25. doi: 10.1111/j.0016-7363.2007.00711.x

Guo, X., Chen, D., & Parker, G. (2019). Flow directionality of pristine meandering rivers is embedded in the skewing of high-amplitude bends and neck cutoffs. *Proceedings of the National Academy of Sciences*, *116*(47), 23448–23454. doi: 10.1073/pnas.1910874116

Gutierrez, R. R., & Abad, J. D. (2014). On the analysis of the medium term planform dynamics of meandering rivers. *Water Resources Research*, *50*(5), 3714–3733. doi: 10.1002/2012WR013358

Harris, C. R., Millman, K. J., van der Walt, S. J., Gommers, R., Virtanen, P., Cournapeau, D., ... Oliphant, T. E. (2020). Array programming with NumPy. *Nature*, *585*(7825), 357–362.

Hickin, E. J., & Nanson, G. C. (1984). Lateral Migration Rates of River Bends. *Journal of Hydraulic Engineering*, *110*(11), 1557–1567. doi: 10.1061/(ASCE)0733-9429(1984)110:11(1557)

Hooke, J. M. (1977). The distribution and nature of changes in river channel pattern. In K. J. Gregory (Ed.), *River channel changes* (pp. 265–280). Wiley-Blackwell, Chichester (UK). (ISBN:978-0471995241)

Hooke, J. M. (2013). River meandering. In E. Wohl & J. F. Shroder (Eds.), *Treatise on geomorphologyy* (Vol. 9, pp. 260–288). Academic Press, San Diego, CA. doi: 10.1016/B978-0-12-374739-6.00241-4

Hooke, J. M., & Harvey, A. M. (1983). Meander changes in relation to bend morphology and secondary flows. In J. D. Collinson & J. J. Lewin (Eds.), *Modern and ancient fluvial systems* (Vol. 6, pp. 121–132). Wiley-Blackwell, Oxford (UK). doi: 10.1002/9781444303773.ch9

Howard, A. D., & Hemberger, A. T. (1991). Multivariate characterization of meandering. *Geomorphology*, *4*(3–4), 161–186. doi: 10.1016/0169-555X(91)90002-R

Howard, A. D., & Knutson, T. R. (1984). Sufficient conditions for river meandering: a simulation approach. *Water Resources Research*, *20*(11), 1659–1667. doi: 10.1029/WR020i011p01659

Ielpi, A., & Ghinassi, M. (2014). Planform architecture, stratigraphic signature and morphodynamics of an exhumed Jurassic meander plain (Scalby Formation, Yorkshire, UK). *Sedimentology*, *61*(7), 1923–1960. doi: 10.1111/sed.12122

Ielpi, A., Lapôtre, M. G. A., Gibling, M. R., & Boyce, C. K. (2022). The impact of vegetation on meandering rivers. *Nature Reviews Earth & Environment*, *3*, 165–178. doi: 10.1038/s43017-021-00249-6

Ikeda, S., Parker, G., & Sawai, K. (1981). Bend theory of river meanders. Part 1. Linear development. *Journal of Fluid Mechanics*, *112*, 363–377. doi: 10.1017/S0022112081000451

Kingma, D. P., & Welling, M. (2022). Auto-encoding variational bayes. *arXiv e-prints*, 12–14. doi: 10.48550/arXiv.1312.6114

Kinoshita, R. (1961). *Investigation of channel deformation in Ishikari river* (Hydraulic laboratory report, hyd no. 325). Tokyo (JPN): Natural Resources Division, Ministry of Science and Technology of Japan.

Kleinhans, M. G., McMahon, W. J., & Davies, N. (2023). What even is a meandering river? A philosophy-enhanced synthesis of multi-level causes and systemic interactions contributing to river meandering. In A. Finotello, P. Durkin, & Z. Sylvester (Eds.), *Meandering Streamflows: Patterns and Processes across Landscapes and Scales* (Vol. 540, pp. 1–52). Wiley-Blackwell, Hoboken (US). doi: 10.1144/SP540-2022-138

Kriegel, H. P., Schubert, E., & Zimek, A. (2017, 8). The (black) art of runtime evaluation: Are we comparing algorithms or implementations? *Knowledge and Information Systems*, *52*, 341-378. doi: 10.1007/s10115-016-1004-2

Lagasse, P. F., Spitz, W. J., Zevenbergen, L. W., & Zachmann, D. W. (2004). *Handbook for predicting stream meander migration.* Washington, D.C. (US): National Cooperative Highway Research Program, report 533. (ISBN: 0-309-088143)

Langbein, W. B., & Leopold, L. B. (1966). *River meanders - Theory of minimum variance* (Professional Paper 422-H). Washington, D.C. (US): U.S. Geological Survey. doi: 10.3133/pp422H

Langendoen, E. J., Mendoza, A., Abad, J. D., Tassi, P., Wang, D., Ata, R., ... Hervouet, J.-M. (2016). Improved numerical modeling of morphodynamics of rivers with steep banks. *Advances in Water Resources*, *93*, 4–14. doi: 10.1016/j.advwatres.2015.04.002

Lanzoni, S. (2022). Morphodynamic Modeling of Alluvial Rivers and Floodplains. In

J. F. Shroder (Ed.), *Reference Module in Earth Systems and Environmental Sciences* (Vol. 10, pp. 83–109). Elsevier. doi: 10.1016/B978-0-12-818234-5.00154-1

Lanzoni, S., & Seminara, G. (2006). On the nature of meander instability. *Journal of Geophysical Research*, *111*, 1–14. doi: 10.1029/2005JF000416

Lazarus, E. D., & Constantine, J. A. (2013). Generic theory for channel sinuosity. *Proceedings of the National Academy of Sciences of the United States of America*, *110*(21), 8447–8452. doi: 10.1073/pnas.1214074110

Lee, G., Gommers, R., Waselewski, F., Wohlfahrt, K., & O'Leary, A. (2019, 4). Pywavelets: A python package for wavelet analysis. *Journal of Open Source Software*, *4*, 1237. doi: 10.21105/JOSS.01237

Leopold, L. B., & Wolman, M. G. (1957). *River channel patterns: Braided, meandering, and straight.* U.S. Government Printing Office. Retrieved from `https://books.google.co.uk/books?id=kUMWcgAACAAJ`

Leopold, L. B., Wolman, M. G., & Miller, J. P. (1964). *Fluvial processes in geomorphology.* San Francisco (US): Freeman. (ISBN: 978-0486685885)

Leuven, J. R. F. W., van Maanen, B., Lexmond, B. R., van der Hoek, B. V., Spruijt, M. J., & Kleinhans, M. G. (2018). Dimensions of fluvial-tidal meanders: Are they disproportionally large? *Geology*, *46*(10), 923–926. doi: 10.1130/G45144.1

Lopez Dubon, S., & Lanzoni, S. (2019). Meandering evolution and width variations: A physics-statistics-based modeling approach. *Water Resources Research*, *55*(1), 76–94. doi: 10.1029/2018WR023639

Mosselman, E. (1998). Morphological modelling of rivers with erodible banks. *Hydrological Processes*, *12*(8), 1357-1370. doi: 10.1002/(SICI)1099-1085(19980630)12:81357::AID-HYP6193.0.CO;2-7

Motta, D., Abad, J. D., Langendoen, E. J., & GarcÃa, M. H. (2012). The effects of floodplain soil heterogeneity on meander planform shape. *Water Resources Research*, *48*(9), 1–17. doi: 10.1029/2011WR011601

Nanson, G. C., & Hickin, E. J. (1983). Channel Migration and Incision on the Beatton River. *Journal of Hydraulic Engineering*, *109*(3), 327–337. doi: 10.1061/(ASCE)0733-9429(1983)109:3(327)

Parker, G., Shimizu, Y., Wilkerson, G. V., Eke, E. C., Abad, J. D., Lauer, J. W., … Voller, V. R. (2011). A new framework for modeling the migration of meandering rivers. *Earth Surface Processes and Landforms*, *36*(1), 70–86. doi: 10.1002/esp.2113

Pedregosa, F., Varoquaux, G., Gramfort, A., Michel, V., Thirion, B., Grisel, O., … Duchesnay, E. (2011). Scikit-learn: Machine learning in Python. *Journal of Machine Learning Research*, *12*, 2825–2830. doi: 10.48550/arXiv.1201.0490

Ran, Y., Liu, Y., Wu, S., Li, W., Zhu, K., Ji, Y., … Huang, P. (2022). A higher river sinuosity increased riparian soil structural stability on the downstream of a dammed river. *Science of The Total Environment*, *802*, 1–10. doi: 10.1016/j.scitotenv.2021.149886

Repasch, M., Scheingross, J. S., Hovius, N., Lupker, M., Wittmann, H., Haghipour, N., … Sachse, D. (2021). Fluvial organic carbon cycling regulated by sediment transit time and mineral protection. *Nature Geoscience*, *14*, 842–848. doi: 10.1038/s41561-021-00845-7

Rosgen, D. L. (1994). A Classification of Natural Rivers. *Catena*, *22*(3), 169–199. doi: 10.1016/0341-8162(94)90001-9

Ruby, U. A., Theerthagiri, P., Jacob, I. J., & Vamsidhar, Y. (2020, 8). Binary cross entropy with deep learning technique for image classification. *International Journal of Advanced Trends in Computer Science and Engineering*, *9*, 5393-5397. doi: 10.30534/ijatcse/2020/175942020

Russell, C. E., Mountney, N. P., Hodgson, D. M., & Colombera, L. (2018). A novel approach for prediction of lithological heterogeneity in fluvial point-bar deposits from analysis of meander morphology and scroll-bar pattern. In M. Ghinassi, L. Colombera, N. P. Mountney, A. J. H. Reesink, & M. Bateman (Eds.), *Fluvial Meanders and Their Sedimentary Products in the Rock Record* (Vol. 48, pp. 385–418). Wiley-Blackwell.

doi: 10.1002/9781119424437.ch15

Santini, W., Martinez, J.-M., Espinoza-Villar, R., Cochonneau, G., Vauchel, P., Moquet, J.-S., ... Guyot, J.-L. (2015, 11-14 December). Sediment budget in the Ucayali River basin, an Andean tributary of the Amazon River. In *Proceedings of the International Association of Hydrological Sciences 2014 - Sediment Dynamics from the Summit to the Sea* (Vol. 367, pp. 320–325). New Orleans, Louisiana (USA). doi: 10.5194/piahs-367-320-2015

Savitzky, A., & Golay, M. J. E. (1964). Smoothing and Differentiation of Data by Simplified Least Squares Procedures. *Analytical Chemistry*, *36*(8), 1627–1639. doi: 10.1021/ac60214a047

Schumm, S. A. (1985). Patterns of alluvial rivers. *Annual Review of Earth and Planetary Sciences*, *13*, 5–27. doi: 10.1146/annurev.ea.13.050185.000253

Schwenk, J., & Foufoula-Georgiou, E. (2016). Meander cutoffs nonlocally accelerate upstream and downstream migration and channel widening. *Geophysical Research Letters*, *43*, 12437–12445. doi: 10.1002/2016GL071670

Schwenk, J., Khandelwal, A., Fratkin, M., Kumar, V., & Foufoula-Georgiou, E. (2017). High spatiotemporal resolution of river planform dynamics from landsat: The RivMAP toolbox and results from the Ucayali River. *Earth and Space Science*, *4*(2), 46–75. doi: 10.1002/2016EA000196

Schwenk, J., Lanzoni, S., & Foufoula-Georgiou, E. (2015). The life of a meander bend: Connectingshape and dynamics via analysis of anumerical model. *Journal Geophysical Research: Earth Surface*, *120*, 690–710. doi: 10.1002/2014JF003252

Seminara, G., Lanzoni, S., & Tambroni, N. (2023). *Theoretical morphodynamics: River meandering*. Florence University Press, Florence.

Seminara, G., & Tubino, M. (1992). Weakly nonlinear-theory of regular meanders. *Journal of Fluid Mechanics*, *244*, 257-288. doi: 10.1017/S0022112092003069

Seminara, G., Zolezzi, G., Tubino, M., & Zardi, D. (2001). Downstream and upstream influence in river meandering. part 2. planimetric development. *Journal of Fluid Mechanics*, *438*, 213–230. doi: 10.1017/S0022112001004281

Sgarabotto, A., Bellizia, E., Finotello, A., D'Alpaos, A., Lanzoni, S., Boaga, J., ... Ghinassi, M. (2024). Reconstructing sediment distribution in meandering river deposits through a simplified numerical modelling approach, with applications to the Holocene deposits of the Venetian Plain (Italy). In A. Finotello, P. R. Durkin, & Z. Sylvester (Eds.), *Meandering Streamflows: Patterns and Processes across Landscapes and Scales* (Vol. 540, pp. 1–21). London: The Geological Society of London. doi: 10.1144/SP540-2022-220

Simons, D. B., & Richardson, E. V. (1966). *Resistance to Flow in Alluvial Channels* (Geological Survey Professional, Paper 422J). Washington D.C. (US): US Government Printing Office.

Sun, X., Shiono, K., Rameshwaran, P., & Chandler, J. H. (2010). Modelling vegetation effects in irregular meandering river. *Journal of Hydraulic Research*, *48*(6), 775-783. doi: 10.1080/00221686.2010.531101

Sylvester, Z., Durkin, P. R., & Covault, J. A. (2019). High curvatures drive river meandering. *Geology*, *47*(10), 263–266. doi: 10.1130/G45608.1

Tary, J. B., Herrera, R. H., & van der Baan, M. (2018). Analysis of time-varying signals using continuous wavelet and synchro squeezed transforms. *Philosophical Transaction of the Royal Society A*, *376*(20170254), 1–16. doi: 10.1098/rsta.2017.0254

Tschannen, M., Bachem, O., & Lucic, M. (2018). Recent advances in autoencoder-based representation learning. *Computing Research Repository*, *abs/1812.05069*. doi: 10.48550/arXiv.1812.05069

van der Walt, S., Schönberger, J. L., Nunez-Iglesias, J., Boulogne, F., Warner, J. D., Yager, N., ... Yu, T. (2014). scikit-image: image processing in Python. *PeerJ*, *2*, 1–18. doi: 10.7717/peerj.453

Vermeulen, B., Hoitink, A. J. F., Zolezzi, G., Abad, J. D., & Aalto, R. (2016). Multiscale structure of meanders. *Geophysical Research Letters*, *43*(7), 3288–3297. doi: 10.1002/2016GL0682387

Weisscher, S. A. H., Shimizu, Y., & Kleinhans, M. G. (2019). Upstream perturbation and floodplain formation effects on chute-cutoff-dominated meandering river pattern and dynamics. *Earth Surface Processes and Landforms*, *44*(11), 2156–2169. doi: 10.1002/esp.4638

Wohl, E., Lane, S. N., & Wilcox, A. C. (2015). The science and practice of river restoration. *Water Resources Research*, *51*(8), 5974–5997. doi: 10.1002/2014WR016874

Wu, F.-C., Shao, Y.-C., & Chen, Y.-C. (2011). Quantifying the forcing effect of channel width variations on free bars: morphodynamic modelling based on characteristic dissipative Galerkin scheme. *Journal of Geophysics Research*, *116*(F3), 1–20. doi: 10.1029/2010JF001941

Yan, N., Colombera, L., & Mountney, N. P. (2021). Controls on fluvial meander-belt thickness and sand distribution: Insights from forward stratigraphic modelling. *Sedimentology*, *68*(5), 1831–1860. doi: 10.1111/sed.12830

Zolezzi, G., & Güneralp, I. (2015). Continuous wavelet characterization of the wavelengths and regularity of meandering rivers. *Geomorphology*, *252*, 98–111. doi: 10.1016/j.geomorph.2015.07.029

Zolezzi, G., Luchi, R., & Tubino, M. (2009). Morphodynamic regime of gravel bed, single-thread meandering rivers. *Journal of Geophysical Research: Earth Surface*, *114*, 1–14. doi: 10.1029/2007JF000968

Zolezzi, G., Luchi, R., & Tubino, M. (2012). Modelling morphodynamic processes in meandering rivers with spatial width variations. *Review Geophysics*, *50*(4), 1–24. doi: 10.1029/2012RG000392

Zolezzi, G., & Seminara, G. (2001). Downstream and upstream influence in river meandering. Part 1. General theory and application to overdeepening. *Journal of Fluid Mechanics*, *438*, 213–230. doi: 10.1017/S0022112001004281